JGR Atmospheres

RESEARCH ARTICLE
10.1029/2020JD032606

Key Points:
- Storm initiation occurred along a northwest-southeast oriented convergence zone and finally organized into an MCS with a bow-echo
- Two low-level mesoscale vortices, one overland and one over the East China Sea, set up the strong convergence zone
- An earlier MCS plays key roles in generating and enhancing the vortex over sea via baroclinic vorticity generation at the edge of its rearward spreading cold pool

Supporting Information:
- Supporting Information S1

Correspondence to:
M. Xue,
mxue@ou.edu

Citation:
Luo, L., Xue, M., & Zhu, K. (2020). The initiation and organization of a severe hail-producing mesoscale convective system in East China: A numerical study. *Journal of Geophysical Research: Atmospheres*, *125*, e2020JD032606. https://doi.org/10.1029/2020JD032606

Received 12 FEB 2020
Accepted 17 JUN 2020
Accepted article online 22 JUL 2020

Author Contributions:
Conceptualization: Liping Luo, Ming Xue
Data curation: Liping Luo
Formal analysis: Liping Luo, Ming Xue
Funding acquisition: Ming Xue
Investigation: Liping Luo, Ming Xue
Methodology: Liping Luo, Ming Xue, Kefeng Zhu
Project administration: Ming Xue
Resources: Liping Luo, Ming Xue
Software: Liping Luo, Ming Xue
Supervision: Ming Xue
Validation: Liping Luo, Ming Xue, Kefeng Zhu
Visualization: Liping Luo
Writing - original draft: Liping Luo
Writing – review & editing: Liping Luo, Ming Xue, Kefeng Zhu

The Initiation and Organization of a Severe Hail-Producing Mesoscale Convective System in East China: A Numerical Study

Liping Luo[1,2,3], Ming Xue[1,4], and Kefeng Zhu[1]

[1]Key Laboratory of Mesoscale Severe Weather/Ministry of Education and School of Atmospheric Sciences, Nanjing University, Nanjing, China, [2]College of Oceanography, Hohai University, Nanjing, China, [3]Southern Marine Science and Engineering Guangdong Laboratory (Zhuhai), Zhuhai, China, [4]Center for Analysis and Prediction of Storms and School of Meteorology, University of Oklahoma, Norman, OK, USA

Abstract The initiation and organization of a long-duration hail-producing mesoscale convective system (MCS) in eastern China are investigated using convection-allowing simulations at 3-km grid spacing with the Advanced Regional Prediction System. The lifecycle of this MCS is characterized by two stages. In the first stage, a series of convective storms are initiated along the northwest border of Jiangsu Provinces. These storms organize into a northwest southeast line as they moved southeastward, eventually organizing into an eastward moving bow-echo structure during the second stage. Our analyses show that the storms initiate along a northwest-southeast oriented convergence boundary set up between two low-level mesoscale vortices, one to the northwest of Jiangsu Province and one over the East China Sea. Comparisons between the fake-dry and control simulations show that the rearward (westward) spreading of a cold pool from another MCS proceeding the hail-producing MCS plays a key role in generating and enhancing the vortex over Eastern China Sea. The tilting of baroclinically generated horizontal vorticity along the edge of the cold outflow creates a cyclonic and anticyclonic vortex couplet. The cyclonic vortex becomes the dominant East China Sea vortex as it is superposed onto the background cyclonic circulation. This cold outflow-induced vortex also has strong impacts on the later organization of the hail-producing MCS, leading to the eventual establishment of a bow-echo structure. Finally, a three-stage conceptual model for the initiation and organization of the long-lasting multicellular MCS is proposed, and the understanding on the complex interactions between two MCSs will be helpful to operational forecasters.

1. Introduction

China is a country that is frequently affected by severe convective weather, such as heavy precipitation, damaging winds, hail, typhoons, and occasional tornadoes (e.g., Feng & Zhao, 2015; Luo et al., 2018; Meng et al., 2012; Xue et al., 2016; Zhu & Xue, 2016). Some studies have shown increased tendencies in the frequency of severe weather over Eastern China, especially in the middle and lower reaches of the Yangtze River, where the population is dense (Li et al., 2016; Zhang & Zhai, 2011).

Organized convection such as mesoscale convective systems (MCSs) accounts for a significant portion of severe weather including heavy precipitation, strong winds and hail in China (Luo et al., 2013). Given their damaging potential, understanding the initiation of convective storms and their organization into MCSs is of both theoretical and practical importance. Over the recent years, convective initiation (CI) has received increasing attention (Bai et al., 2019; Huang et al., 2017; Su & Zhai, 2016; Wang et al., 2014, 2016). For example, Wang et al. (2016) investigated CI due to topographically dynamic and thermodynamic effects and its interactions with weak environmental flows over the Dabie Mountain in eastern China for a real case in the Mei-yu season via numerical simulations. More recently, Huang et al. (2017) conducted a statistical survey of isolated CI over central eastern China (CEC) with the Chinese operational geostationary satellite Fengyun-2E and ground-based weather radars measurements; the initiation of a severe squall line over CEC was also explored based on radar observations and idealized simulation in Bai et al. (2019), which occurred due to the interaction between intersecting gust fronts and a quasi-stationary dryline. Besides, CI was also an important subject of the International H_2O Project (IHOP) field experiment (Weckwerth et al., 2004). Numerical studies on CI cases from IHOP include Xue and Martin (2006), Liu and Xue (2008), and Wang and Xue (2012, 2018). A rich array of observations during the Plains Elevated Convection At Night (PECAN) field campaign over the Great Plains is also helpful for better understanding CI of nocturnal MCSs and their relationship with the environment (Geerts et al., 2017). Various forcing mechanisms for CI have been studied, including forcings by surface-based convergence lines and initiation by elevated features. For surface-based CI, boundary layer forcings are often associated with synoptic fronts, gust fronts, dry line, boundary layer horizontal convective rolls, or other forms of convergence lines (Barthlott et al., 2010; Cai et al., 2010; Fabry, 2006; Lee et al., 2016; Wang & Xue, 2012; Xue & Martin, 2006; Ziegler et al., 2010), while elevated CI is generally triggered by convergence or confluent features off the ground (Corfidi et al., 2008; Geerts et al., 2017; Marsham et al., 2011; Reif & Bluestein, 2018; Wilson et al., 2018). Convection is also often initiated by orographic forcing (Lean et al., 2009; Rasmussen & Houze, 2016; Xu et al., 2012) and sometimes by gravity wave or bore activities (e.g., Parsons et al., 2019; Su & Zhai, 2016). Understanding CI for individual cases is often challenging due to the wide variety of possible forcing mechanisms and the lack of high-resolution observations. The exact forcing mechanism responsible for CI in a specific case is often difficult to ascertain, especially when multiple mesoscale processes and their interactions are involved (Browning et al., 2007; Marsham et al., 2011; Weckwerth & Parsons, 2006).

Another important issue in MCS research is the relationship between MCSs and the complex mesoscale heterogeneities within which they evolve (Wheatley & Trapp, 2008). Several studies including both observations and mesoscale model simulations were performed to investigate the impacts of mesoscale heterogeneities of soil moisture, orographic forcing, and cold pools, on MCSs evolution and precipitation (e.g., Duffourg et al., 2016; Frye & Mote, 2010; Gerken et al., 2018; Koukoula et al., 2019; Taylor & Ellis, 2006; Taylor, Gounou, et al., 2011; Taylor, Parker, et al., 2011; Xu et al., 2012). It was concluded that the variations in soil moisture play a substantial role in determining the sensible and latent heat fluxes within the boundary layer (Adler et al., 2011). The mesoscale heterogeneities often generate secondary circulations, which in turn may modify the convection environment and trigger convection (Adler et al., 2011; Trier et al., 2004). For example, Xu et al. (2012) noted that the cold pool from previous precipitation over southwest Taiwan Island and adjacent ocean acted to effectively extend the orographic lifting effect of Taiwan into the ocean, indirectly affecting continuous convective initiation over the upstream ocean. More recently, based on extensive numerical sensitivity experiments for four convective precipitation flooding events over the Gard region of southern France, Koukoula et al. (2019) elucidated the complex feedback mechanism between soil moisture and convective precipitation. Their results are consistent with previous studies that show strong sensitivities between the feedback of mesoscale heterogeneities on the initiation and evolution of MCSs (Taylor & Ellis, 2006).

In more recent years, with the continuous increase in computing power, real-case convection-permitting/resolving simulations of MCSs at grid spacings of 1–4 km have become common (e.g., Duffourg et al., 2016; Grilli et al., 2015; Luo et al., 2014; Xu et al., 2017). Among them, Luo et al. (2014) used convection-permitting simulations to investigate the linkage between early morning precipitation and the evolution of MCS at night along a Meiyu front in eastern China. Duffourg et al. (2016) is an example of a high-resolution simulation for MCSs developing offshore over the French coastal regions. Realistic convection-permitting/resolving model simulations, combined with high-resolution observations, provide us great opportunities to gain a more in-depth understanding of the initiation and organization of MCSs. Besides, when mesoscale heterogeneities are considered, the processes involved in different cases that occur in different regions and under different synoptic scale conditions can be very different and therefore require specific studies. As the northern and eastern China are most frequently affected by severe convection associated with upper-troposphere cutoff lows from April through June; the cutoff lows often migrate southeastward to the east coast of China (Lian et al., 2016; Xie & Bueh, 2015), where population is the most dense. Thus, an in-depth understanding of mesoscale heterogeneity and its interactions with deep convection is clearly of great importance for more accurate operational forecasting. The present study focuses on the initiation and later organization of a long-lasting hail-producing MCS that occurred over Jiangsu Province in eastern China on 28 April 2015 under the influence of a cutoff low. The complex interactions between the hail-producing MCS and another proceeding MCS make this case unique.

According to the severe weather reports from the Chinese Meteorological Administration, this MCS was a prolific producer of chicken egg-sized hailstones (3–5 cm in diameter), intense lightning, and damaging surface winds (>23 m s^{-1}). This MCS occurred under a deep, semi-permanent upper-level East Asian trough (EAT), which could be traced back to 26 April 2015. Convection first formed at the northwestern border of Jiangsu Province. The storms organized into an MCS and moved southeastward, sweeping through much of the Jiangsu Province and eventually evolved into a bow echo. This MCS was proceeded by another MCS that developed on the evening of 27 April over eastern China and moved eastward into the East China Sea before the hail-producing MCS developed. This case was quite successfully simulated by Luo et al. (2018), utilizing multimoment microphysics schemes that predict different numbers of particle size distribution moments. Luo et al. (2018) focused on examining the skill of explicit hail prediction with different microphysics schemes and the reasons for the hail prediction differences. The results indicate that the three-moment Milbrandt and Yau scheme (Milbrandt & Yau, 2005) reproduces the storm evolution and hail distribution the best compared with available observations. The study did not, however, examine the initiation and organization processes of the hail-producing MCS, which is the focus of this study.

The main objectives of this study are twofold: (i) to investigate the mechanisms governing the initiation and organization of the long-lasting hail-producing MCS of 28 April 2015 over Jiangsu Province, China, and (ii) to investigate the possible linkage between the proceeding MCS (referred to as PMCS hereafter) and the primary hail-producing MCS (HMCS hereafter) of interest. Convective initiation in this study refers to the initiation of initial storm cells, defined as the first occurrence of a radar reflectivity reaching 35 dBZ from an isolated convective storm and the initiated storm lasts over 30 min similarly from several previous studies (e.g., Bai et al., 2019; Huang et al., 2017; Walker et al., 2012). The cold pool is identified based on surface potential temperature that is more than 2 K colder than the environment (Maurer et al., 2017). The leading edge of the cold pool outflow is defined as the gust front, which is accompanied by a sharp temperature gradient of more than 2 K. Data sets used herein include observed radar reflectivity, satellite imageries, surface rainfall observations, and model simulations at 3-km grid spacing.

The remainder of this paper is organized as follows. Section 2 provides an overview of the synoptic scale conditions near the time of the 28 April 2015 MCS, and the evolution of HMCS and PMCS in terms of infrared satellite cloud top temperature. Section 3 briefly documents the simulation model setup and verifies the control simulation against observations. Section 4 examines the mechanisms of the initiation and organization of HMCS. The effect of PMCS on the development of HMCS is investigated with the aid of a sensitivity experiment in which the PMSC is suppressed by removing latent heating and cooling from microphysics. A summary and conclusions, including a conceptual model of the initiation and organization of the main MCS and its linkage with PMCS, are presented in the final section.

2. Case Overview

The synoptic patterns associated with the 28 April 2015 HMCS are shown in Figures 1 and 2, based on the National Centers for Environmental Prediction (NCEP) Operational Global Forecast System (GFS) final analyses. Before and during the lifespan of this MCS, the northeastern coastal region of China was dominated by a deep, southwestward extending trough at the middle-to-upper levels, which could be traced back to 1200 UTC 26 April 2015 (Figure 1a). In the colder half of the year, the coastal region of East Asian is often occupied by a deep, semipermanent trough that is commonly known as the East Asian Trough (EAT) (Chen et al., 2018; Song et al., 2016; Wang et al., 2009). At the time, Jiangsu Province was located ahead of the upper-level trough line and at the front-left exit region of the East Asia upper-tropospheric jet stream (EAJS) (Figure 2a). Positive vorticity advection from this EAT and the upper-level divergence associated with the EAJS contributed together to destabilize the atmosphere, providing a favorable synoptic environment for the MCS. With a significant increase in the amplitude of the EAT, two cold-core cutoff lows (hereinafter COLs, denoted L) formed within the EAT by 0600 UTC 28 April at 500 hPa (Figure 1e). The COL on the west side at 500 hPa was initially stronger and moved southward from northern Hebei Province (~41°N) at 1800 UTC 27 April (Figure 1c) to northern Jiangsu Province (~34°N) by 1200 UTC 28 April (Figure 1f). This southward migration of the COL was accompanied by a southward excursion of cold air to over Jiangsu Province at the middle levels (Figures 1c–1e). During the period, the eastern COL moved slowly eastward, from over the eastern tip of the Shandong Peninsula (Figure 1c) to over the East China Sea (Figure 1f, and see Figure 4 for location references). The COLs belong to a class of cold vortices that are responsible for a significant portion of severe weather over northeastern China (Zhang & Li, 2009).

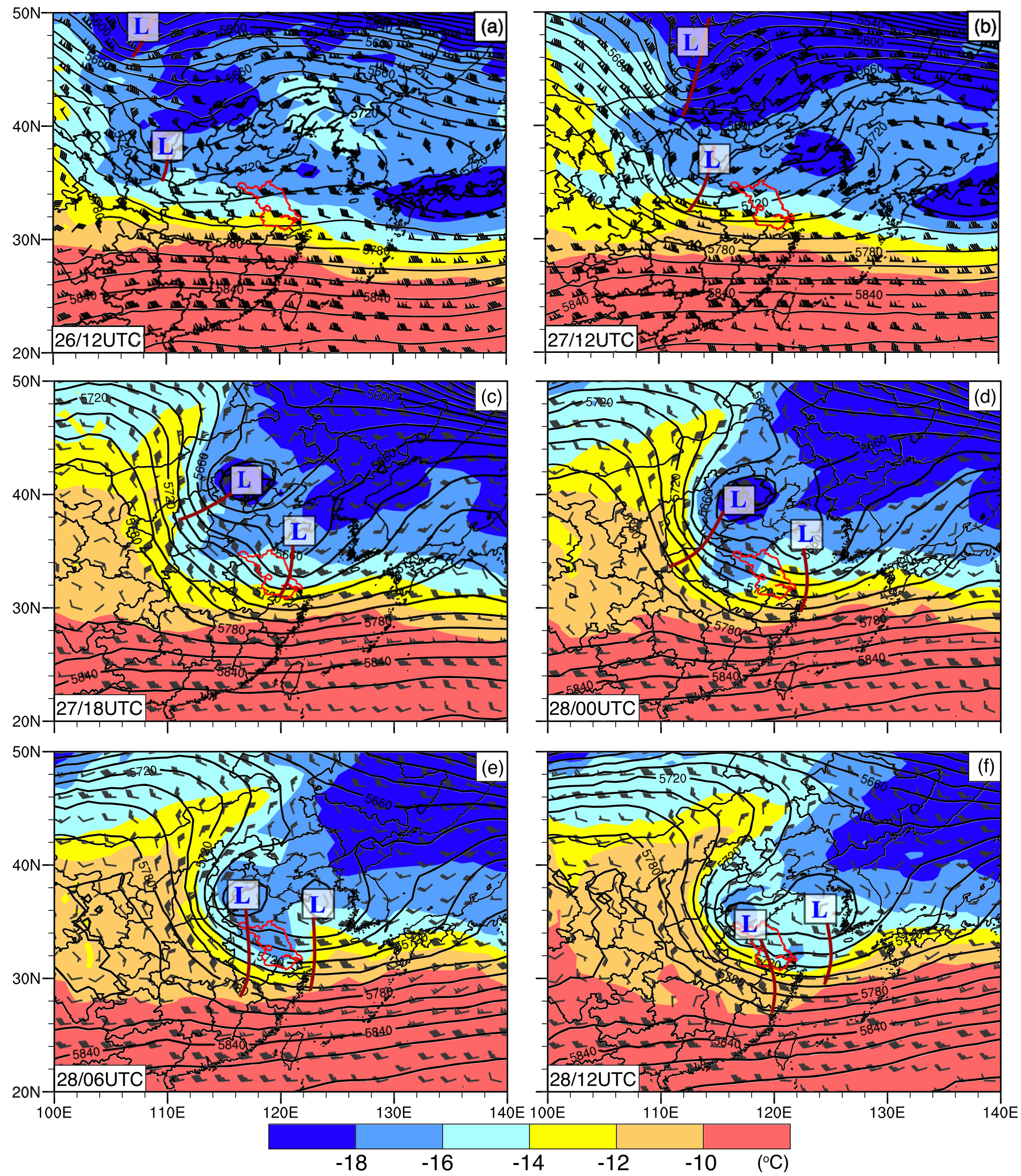

Figure 1. Synoptic features at 500 hPa at (a) 1200 UTC 26 April, (b) 1200 and (c) 1800 UTC 27 April, and (d) 0000 UTC, (e) 0600 UTC, (f) 1200 UTC 28 April, 2015, showing wind bars (one full barb denotes 2.5 m s^{-1}), temperature (shaded, interval of 2°C), and geopotential height (solid black contours, gpm). The thick solid brown lines within each panel indicate trough lines and the blue uppercase L denotes the cut-off lows at 500 hPa. Jiangsu Province is outlined by the red solid line in each panel.

Studies have shown that owning to their high positive potential vorticity, COLs can induce low-level cyclonic circulations and often promote severe convection, especially when they move over regions with potentially unstable low-level flows (e.g., Hu et al., 2010; Knippertz & Martin, 2007; Tsai et al., 2010). The coupling of midlevel COLs and low-level cyclonic circulation was clearly evident for the current case. At 0600 UTC 28 April, the western and eastern COLs at ~37°N and ~36.5°N respectively at the 500-hPa level (Figure 2b) corresponded to clearly defined cyclonic circulations at the 850-hPa level (Figure 2c) and the surface (Figure 2d). Warm (>28°C) low-level southwesterly flows associated with the western COL over Anhui and Jiangsu Provinces (see Figure 1) and the much colder (<16°C) northeasterly flows as part of the cyclonic circulation over the East China Sea set up a strong convergence zone from the northwest through southeast Jiangsu Province at the low levels (Figures 2c and 2d). Along and to the southwest of the convergence zone,

10.1029/2020JD032606

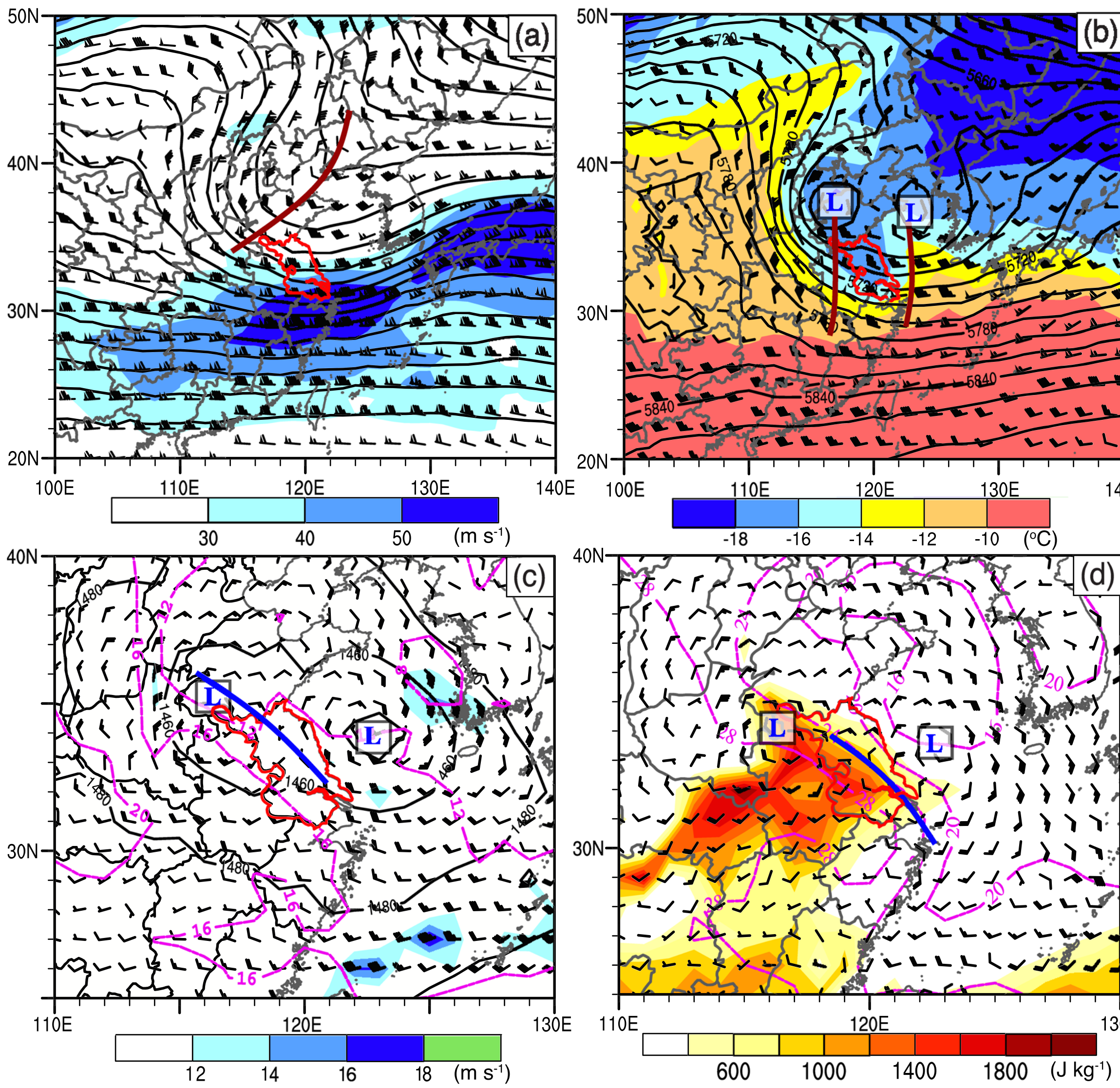

Figure 2. Synoptic features at 0600 UTC 28 April close to the time of the hail-producing MCS initiation, at the levels of (a) 200, (b) 500, (c) 850, and (d) 1,000 hPa, showing wind barbs (one full barb denotes 2.5 m s^{-1}), geopotential height (black solid lines; gpm), total horizontal wind speed in (a) and (c) (shaded), temperature in (b) (shaded, °C), in (c) and (d) (magenta dash contours, °C), and CAPE in (d) (shaded, J kg^{-1}). The thick solid brown and blue lines in (a)–(d) denote the trough and shear lines, respectively. Jiangsu Province is outlined by red solid line in each panel, and the uppercase L indicates the low-level mesoscale vortex. Note the difference in the size of domains plotted in upper and lower panels.

moderately high convective available potential energy (CAPE, >1,500 J kg^{-1}) was present (Figure 2d); coupled with destabilizing upper-level circulations, favorable conditions for severe convection existed. Moreover, as shown in Figure 4 of Luo et al. (2018), the sounding extracted at 0600 UTC at 34°N, 117°E from NCEP GFS Final analysis at 1° resolution has a CAPE of 1,433 J kg^{-1} and a weak capping inversion between 850 and 800 hPa (a convective inhibition of −5 J kg^{-1}). There exists strong low to midlevel vertical wind shear (~24.5 m s^{-1}), which helps to maintain the long-lasting severe convection (Luo et al., 2018; Weisman & Klemp, 1984). The air above the inversion layer is cold and dry, resulting from the midlevel cold advection directly over Jiangsu Province, and this cold dry layer was superimposed on warm moist layer near the surface. Such conditions are favorable for large hailstones reaching the surface due to reduced melting of hail (Costa et al., 2001; Luo et al., 2017).

A time sequence of satellite infrared cloud top brightness temperature (TBB) imageries from the Chinese operational geostationary satellite FengYun 2E (FY-2E) in Figure 3 show the evolution of convective systems in this event. At 1800 UTC 27 April, over western Shandong Province, some low clouds were present while

10.1029/2020JD032606

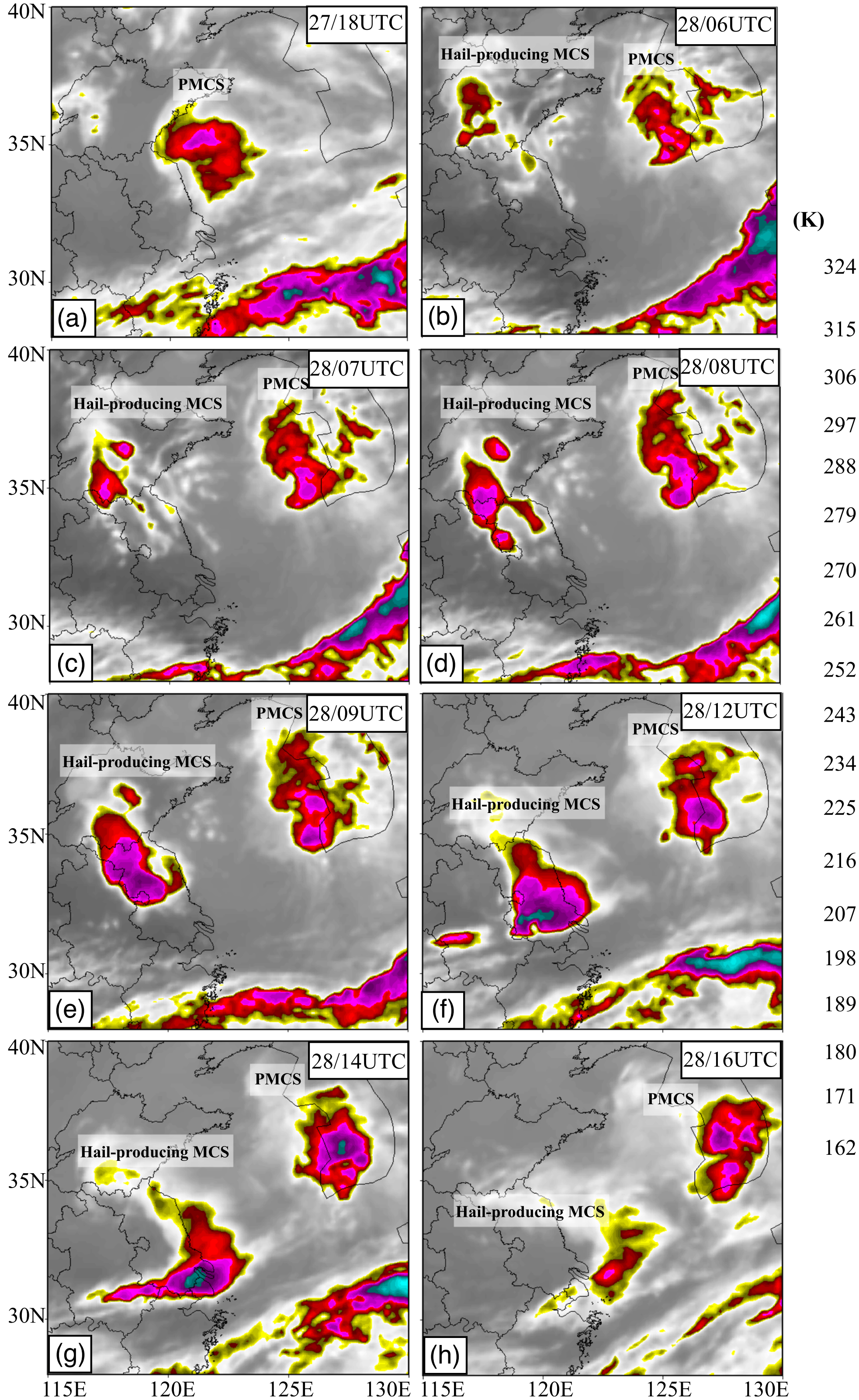

Figure 3. (a–h) Satellite infrared cloud top brightness temperature (TBB) at selected times covering both the lifespans of preceding convective system and hail-producing multicellular convective system, which are denoted as PMCS and hail-producing MCS.

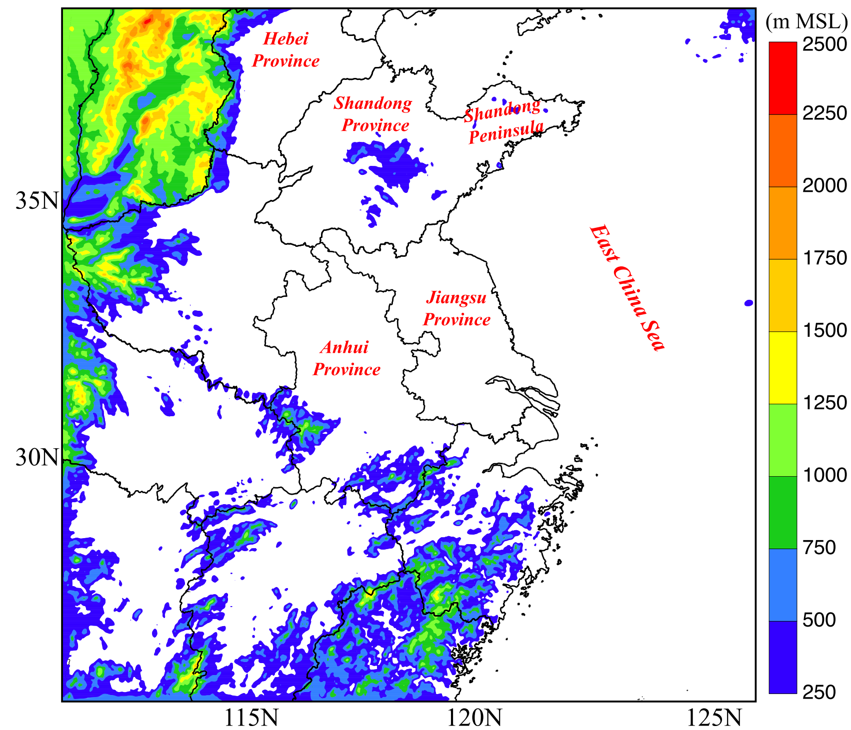

Figure 4. Model domain of the 3-km grid spacing for the simulations. Terrain elevation (m) is shaded. Provinces of Hebei, Shandong, Jiangsu, and Anhui, Shandong Peninsula and the East China Sea are labeled in red. Note that the elevation in most of Jiangsu Province is only 10–20 m MSL.

the main system at this time was a significant MCS with TBB lower than 225 K off the coast of Jiangsu Province over the East China Sea (Figure 3a). The latter was what we referred to as PMCS as it occurred before the hail-producing MCS. As will be discussed later, PMCS had important roles to play in the development and evolution of HMCS.

By 0600 UTC (1400 LST) 28 April, the convection over western Shangdong Province became deeper but was still not well organized while PMCS had moved to near the western coast of the Korean Peninsula (Figure 3b). Within the next hour, deep convection (TBB < 225 K) near the northwest border of Jiangsu and Shangdong Provinces quickly developed while the convection to its north weakened. The sign of a line of initiating clouds to the south along the Jiangsu and Anhui border was evident (Figure 3c). By 0800 UTC, deep convection formed along these initiating clouds while the main body of convection expanded in area coverage (Figure 3d). By 0900 UTC, this convective system became well organized, the cloud top with TBB < 225 K was occupying most of the northern Jiangsu Province (Figure 3e).

Over the next 3 hr, HMCS moved southward in western Jiangsu Province and underwent reorganization as well. The north-south oriented HMCS changed from a more north-south direction to a more east-west direction, and TBB < 216 K appeared in a narrow band in an east–west orientation (Figure 3f). Over the next 2 hr, more changes occurred with the structure of the overall MCS, and deepest convection was now found near the east coast. The MCS gained a “comma” shape, with a tail extending westward into Anhui Province. As will be seen later, this occurred as the system started to move eastward under the influence of low-level flows, part of which is was related to the cyclonic circulation associated with the western COL. After 1400 UTC, the main part of HMCS moved off the coast, and the entire MCS became mostly dissipated by 1,600 UTC (0000 LST). Over the entire period, PMCS slowly moved eastward over the Korean Peninsula, and more or less maintained its intensity (Figures 3b–3h).

It was suggested that the strong low-level convergence between the two cyclonic circulations may have important roles to play in the initiation and organization of HMCS. At the same time, HMCS was proceeded by a major PMCS to its east. One may ask, what role, if any, did PMCS play in the initiation and evolution of the ensuing HMCS? Did PMCS modify the low-level circulation that may affect the subsequent HMCS? We try to answer these and other questions by examining convection-permitting simulations of this event.

3. Numerical Experiment Configurations and Verification

3.1. Configurations of Numerical Experiments

As reported in Luo et al. (2018), the multiscale processes leading to and being involved in the long-duration hail-producing MCS were simulated at a 3-km grid spacing using the Advanced Regional Prediction System (ARPS; Xue et al., 2000; Xue et al., 2001; Xue et al., 2003) model. ARPS is a three-dimensional, nonhydrostatic, fully compressible mesoscale and storm-scale prediction model using generalized terrain-following vertical coordinates. The simulations are initialized at 1200 UTC 27 April and integrated for 30 hr. The NCEP 1° GFS final analysis at 1200 UTC 27 is used as the initial condition and later analyses at 6-hr intervals are used as the boundary conditions.

A single simulation domain used (Figure 4) covers a $1,500 \times 1,500$ km^2 region using 503×503 grid points in the horizontal, centered at (32.5°N, 118.5°E). The grid has 53 vertical levels with 18 of them located below the 2-km height. The vertical grid spacing ranges from 50 m near the surface to approximately 1,000 m at the model top, stretched using a hyperbolic tangent function (Xue et al., 1995). Fourth-order computational diffusion is used for suppressing numerical noise and subgrid-scale turbulent mixing is parameterized using a 1.5-order turbulence kinetic energy (TKE) scheme with the PBL parameterization of Xue et al. (1996) based on Sun and Chang (1986). A two-layer land surface model is applied to predict the surface temperature and soil moisture content (Pleim & Xiu, 1995). The radiative processes are parameterized using the National Aeronautics and Space Administration (NASA) Goddard Space Flight Center (GSFC) long- and short-wave radiation scheme. For the simulations in this paper, the three-moment Milbrandt and Yau microphysics scheme (Milbrandt & Yau, 2005) is utilized. The control simulation in this paper corresponds to the outer 3 km grid control simulation of Luo et al. (2018) that also used the three-moment Milbrandt and Yau scheme. Because of our interest in the full life cycle of HMCS and the possible linkage between HMCS and PMCS preceding it, we choose to focus on simulations on the larger 3-km grid in this study. On the other hand, Luo et al. (2018) focused exclusively on simulations on the nested 1-km grid to study hail production processes and hail prediction. Even with the larger 3-km grid, the eastward moving PMCS did move out of the eastern boundary later on, but the simulation of PMCS itself at the later stage is not the focus of this study. More details on the model physics and configurations can be found in the ARPS model description papers.

In addition to the control simulation, a sensitivity experiment is performed in which latent heating and cooling from microphysics processes are discarded during the early stage of simulation between 1200 UTC 27 April and 0600 UTC 28 April. Thus, the earlier PMCS is suppressed before HMCS is initialized in the sensitivity experiment. We turned the latent heating and cooling effects back on before HMCS is initiated at 0600 UTC 28 April, so that HMCS can develop in the model. The effect of PMCS on the low-level circulations is thereby isolated so as to study its role in the development and evolution of the later HMCS. We call this simulation "fake dry" simulation because the moist processes and their impacts are effectively turned off during the earlier period.

To establish the credibility of the simulation before analyzing the physical processes based on the simulation output, in the following two subsections, we first verify the 30-hr simulation of HMCS against operational S-band Doppler radar reflectivity observations and the hourly gauge-satellite-merged precipitation product. The precipitation product is at 0.1° spatial resolution from the Chinese Meteorological Data Service Center (referred to as CMORPH _CMDC_0.1° hereafter). CMORPH _CMDC_0.1° is merged from the Chinese automatic stations hourly precipitation observations and the National Oceanic and Atmospheric Administration (NOAA) Climate Prediction Center Morphing (CMORPH) precipitation product at ~8 km every 30 min, covering continental China. CMORPH _CMDC_0.1° has been shown to exhibit reduced bias and random errors compared with the original NOAA CMORPH precipitation product. Shen et al. (2014) noted that the application of improved probability density function and optimal interpolation (PDF-OI) technique incorporating local precipitation data contributes to the improvement of CMORPH _CMDC_0.1°.

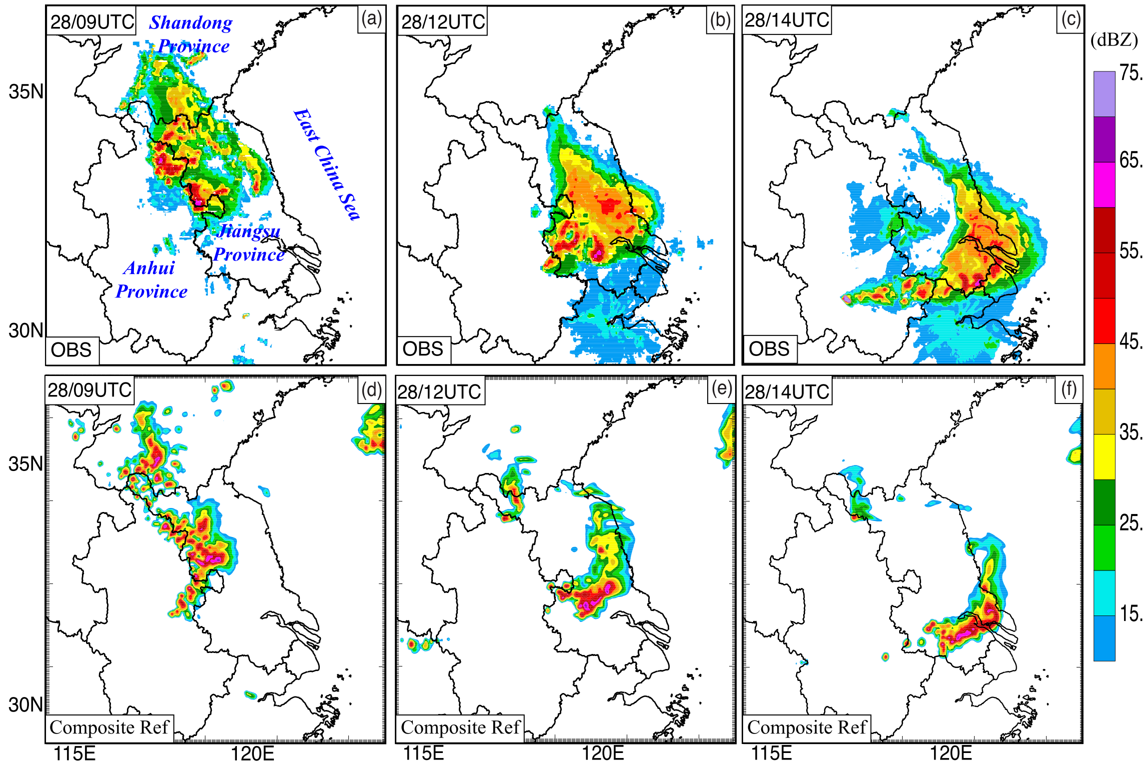

Figure 5. Composite (column-maximum) radar reflectivity fields (dBZ) from (a–c) operational radar observations and (d–f) from the control simulation at 0900, 1200, and 1400 UTC 28 April 2015 during the lifespan of HMCS.

3.2. Radar Reflectivity Verification

Figure 5 compares the radar-observed and model-simulated composite (column-maximum) radar reflectivity during the lifespan of HMCS. This control simulation reproduces the general features of the observed HMCS, including the initiation of initial convective storms along the northwestern border of Jiangsu Province, their organization into an MCS during the southeastward propagation, and the eventual evolution of the MCS into an eastward extending bow-shaped echo with a long westward extending tail (Figure 5). At the later stage, the MCS gains more of an eastward movement and a bow structure in reflectivity develops. Convection is strongest along the leading edge of the bow (Figures 5c and 3g) while other convective cells are initiated and maintained along the outflow boundary extending to the west-southwest (Figure 5c). These general features are captured in the simulation, although the stratiform precipitation region within the MCS is underpredicted compared with the radar observations. Possible reasons for this include too fast sedimentation of large hailstones so that less time is available for rearward advection of hydrometeors (Luo et al., 2018).

Generally speaking, the simulation captures the overall structure and evolution of the MCS reasonably well, although it is not possible to match up the convective cells between the observation and simulation one by one. The simulated MCS is also displaced tens of kilometers to the northeast of the observed system. Considering that the forecast range is more than 24 hr and the initial condition is that of a global model analysis without the assimilation of fine-scale local observations, such simulation results can be considered rather good. Thus, the key physical processes, the main interest of this study, are analyzed based on the simulation results. In fact, using fractions skill score that allows for a certain degree of location error, Luo et al. (2018) shows that this simulation has useful skill in predicting hail fall at the surface. The accumulated precipitation forecast will be examined next.

3.3. Precipitation Forecast Verification

The observed and model simulated 10 hr (from 0600 to 1600 UTC 28 April) accumulated total precipitation, as well as the simulated liquid precipitation fields are presented in Figure 6. The model reproduces the general northwest to southeast elongated rainfall swaths extending to the southeast corner of Jiangsu Province as observed. However, there are quantitative differences between the observation and simulated

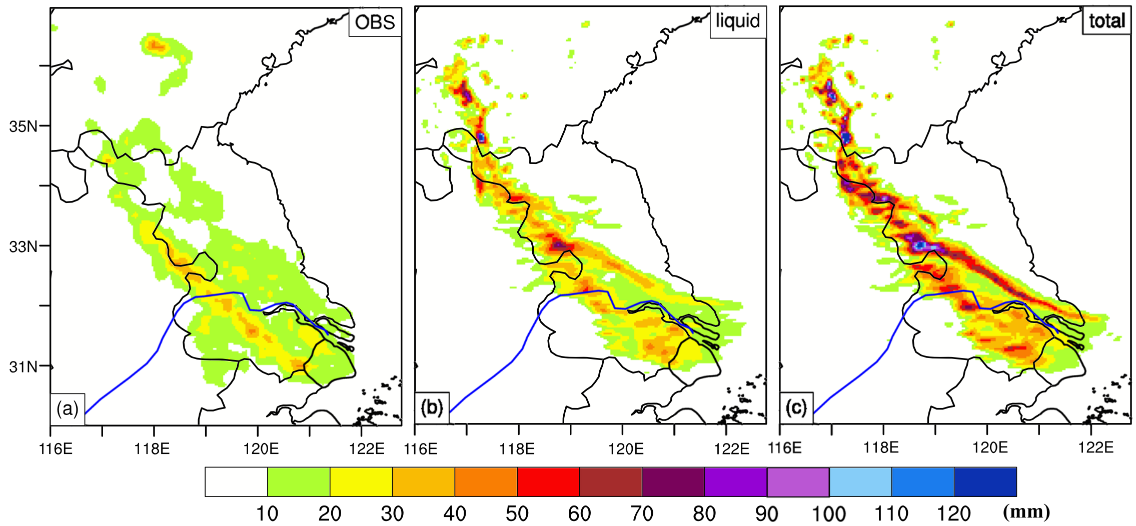

Figure 6. Ten-hour (a) observed surface accumulated precipitation (mm) from 0600 to 1600 UTC 28 April 2015, and (b) corresponding predicted liquid precipitation and (c) total precipitation. The blue solid lines indicate the lower reaches of the Yangtze River.

precipitation, in both intensity and locations when examined in detail. The accumulated total precipitation, including hail mass on the surface, is overpredicted by the model, with the peak values at isolated locations reaching over 120 mm; the simulated precipitation in the northern part is noticeably more intense than observed (Figures 6a and 6c). The simulated liquid precipitation is closer to the observation (Figures 6a and 6b). Note that the precipitation observations from CMORPH _CMDC_0.1° utilized herein have also been compared with other precipitation products, that is, the NOAA CMORPH precipitation products at ~8 km and 0.25° spatial resolution and the Integrated Multi-Satellite Retrievals for Global Precipitation Measurement (IMERG V6) at 0.1° spatial resolution. It is found that there also exists significant discrepancy in the rainfall amount and extent among different precipitation products (not shown), which indicates the uncertainties within the rainfall data sets.

We believe such differences can be due to both model forecast error and rainfall data uncertainty. The rain gauge network has a much lower resolution compared to that of model, the rainfall extremes tend to be underestimated (Molini et al., 2005). Previous studies also found that surface rain gauge measurements can easily underestimate solid precipitation in the presence of strong winds (e.g., Fortin et al., 2008). At the same time, Zhu et al. (2018) noted that 4-km convective-permitting simulations tend to overpredict rainfall in the warm season of China, especially along the coastal regions. Moreover, both the high values of composite radar reflectivity exceeding 60 dBZ along the northwest border of Jiangsu Province (cf. Figure 5a), and the 24-hr severe weather report from the Chinese Meteorological Society (cf. Figure 1 in Luo et al., 2018) show severe hail fall over the northern half of the precipitation region. These are generally consistent with our simulated precipitation pattern.

Given the general agreement between the simulation and observations in the development of HMCS and its surface accumulated precipitation distribution, we will focus on investigating the mesoscale processes connected with the initiation and organization of the MCS in the following sections based on simulation results.

4. HMCS in the Control Simulation

4.1. Initiation and Organization of HMCS

Figures 7 and 8 show the simulated composite (column-maximum) radar reflectivity, surface wind and temperature fields. It is noted that CI first occurred along the northwest border of Jiangsu Province, along a northwest-southeast-oriented convergence zone (Figure 7a). Evidently, this strong convergence zone forms between the southwesterly winds on the south side of the low-level cyclonic circulation or vortex over land and the strong northeasterly flows that are part of the cyclonic circulation or mesoscale vortex located over the East China Sea. The overland vortex is believed to be linked to the western midlevel COL (Figure 2) as discussed earlier. Further south of the overland vortex is a broad area of southwesterly

10.1029/2020JD032606

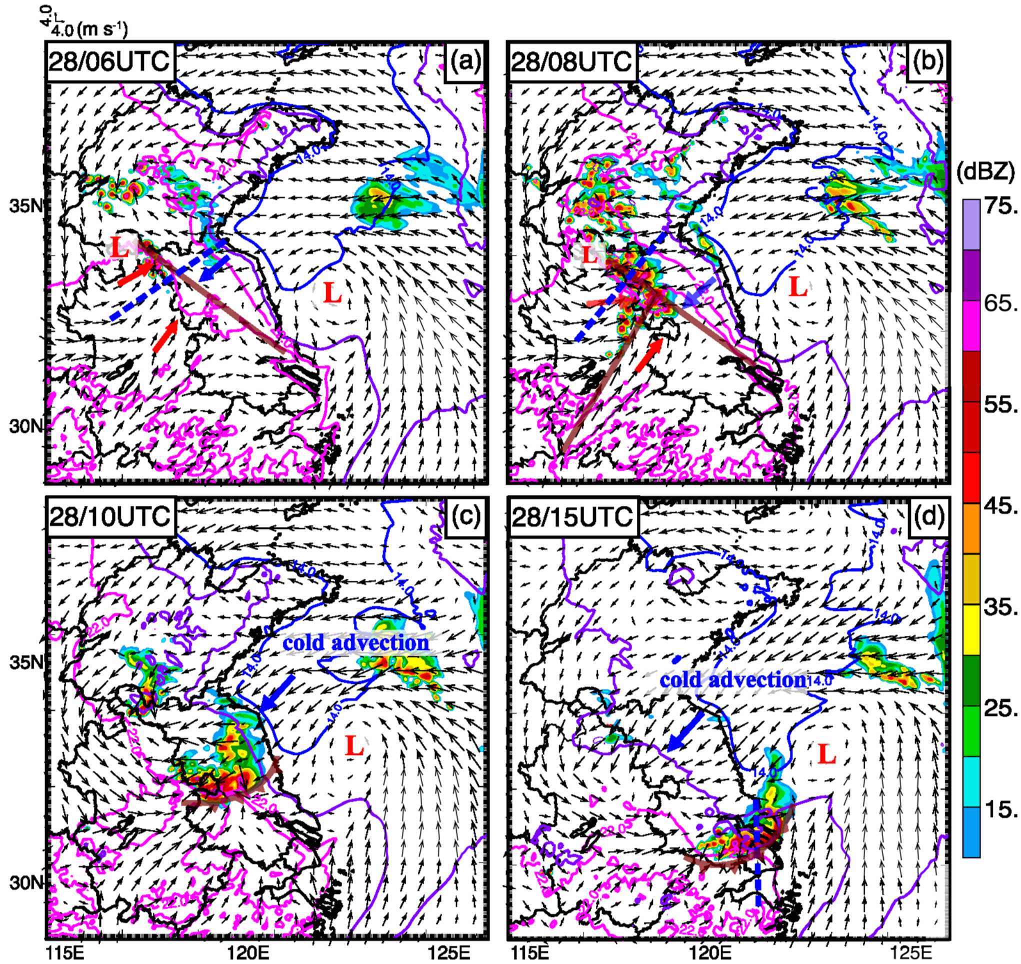

Figure 7. Composite (column-maximum) radar reflectivity (shaded, dBZ), surface wind (vector unit shown in the plots, m s^{-1}) and temperature fields (colored contours, with interval of 4°C) at (a) 0600, (b) 0800, (c) 1100, and (d) 1500 UTC 28 April 2015. The brown solid bold lines in (a) and (b), and (c) and (d) indicate convergence lines and gust fronts, respectively. Label "L" marks the location of the mesoscale vortex over land and over the East China Sea. The bold red and blue arrows indicate key flow features. The bold dashed blue lines within each panel denote the locations of vertical cross sections in Figure 9.

flows that bring in high-CAPE air into the convergence region (cf. Figure 2d) and provide favorable conditions for convection along the convergence line. The vortex over the East China Sea is suggested to be linked to the eastern midlevel COL (Figure 2), although we will show later that it has been modified by PMCS. The northeasterly flows toward the convergence line are relatively cold (Figures 7a, 7b, 8a, and 8b) and are more convectively stable.

After the initiation of initial convective cells, the cells move south-southeastward, more or less along the low-level convergence line while being steered by midlevel northwesterly flows (see Figure 2b). More cells form along the convergence line and the cells grow in size and intensity (Figures 7b and 3e). It is clear that the presence of the low-level convergence zone plays important roles in the initial development and organization of the MCS during this stage of evolution. To further examine whether the simulated convergence line more or less matches observations, surface temperature and wind observations from the Meteorological Information Combine Analysis and Process System (MICAPS) of China Meteorological Administration (CMA) are examined. The simulated convergence zone is generally consistent with observations, although the southern half of the convergence zone is displaced tens of kilometers northeastward from the observations due to forecast position error (not shown). Because the focus of this paper is on physical processes, not quantitative precipitation forecasts, the discrepancies in the simulation should not affect our physical interpretation of results.

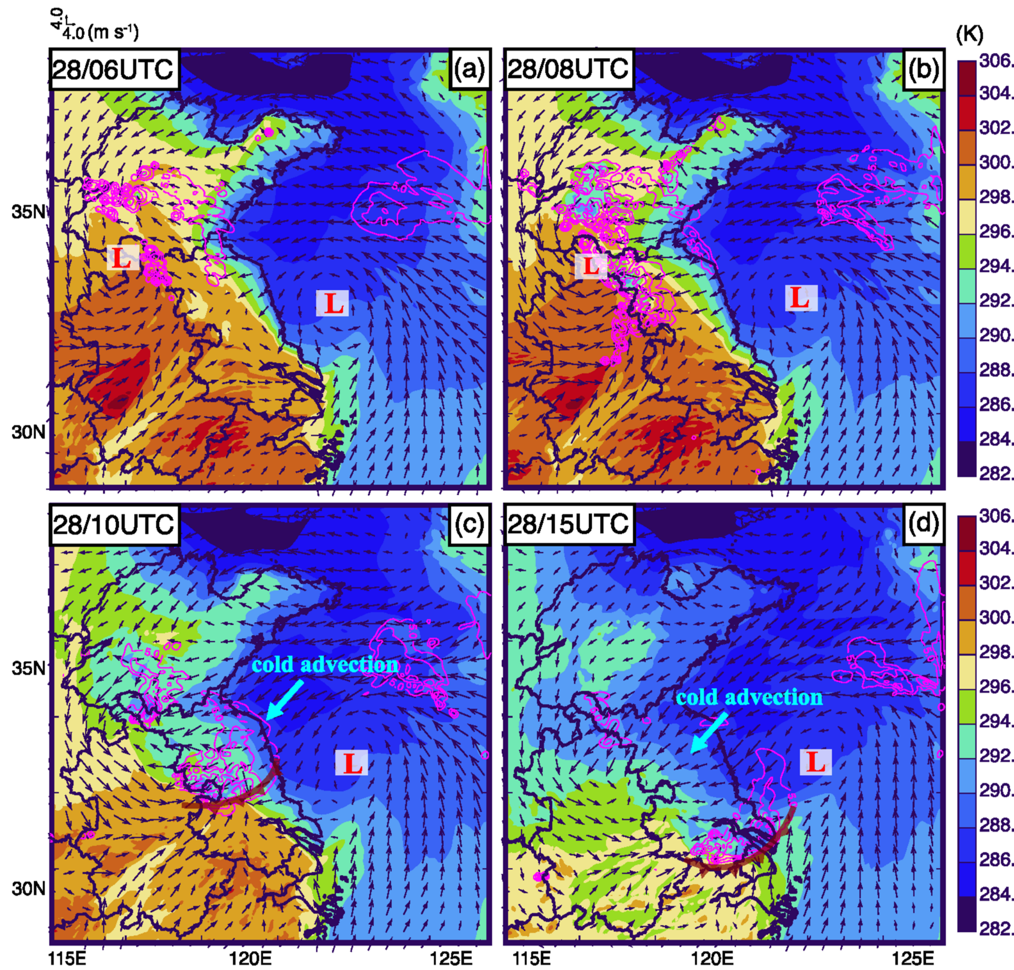

Figure 8. As Figure 7, but surface potential temperature (shaded, with an interval of 2 K), surface wind (vector unit shown in the plots, m s^{-1}), and composite (column-maximum) radar reflectivity (magenta contours, dBZ) at (a) 0600, (b) 0800, (c) 1100, and (d) 1500 UTC 28 April 2015. The brown solid bows in (c) and (d) indicate gust fronts, respectively. Label "L" marks the location of the mesoscale vortex over land and over the East China Sea.

In the control simulation, the convergence zone indicated by the straight brown line in Figures 7a and 7b is apparently responsible for the line of heavy precipitation in the next stage of MCS development. Significant changes occur to the low-level flows between 0800 and 1100 UTC 28 April. The prominent convergence zone between east-northeasterly flows and west-southwesterly flows along the northern Jiangsu-Anhui border at 0800 UTC supports the main convective line (Figure 7b). Several small areas of low potential temperature are present underneath the convective cells (Figures 8a and 8b). HMCS becomes disorganized by 1100 UTC (Figure 7c) as the vortex over the East China Sea moves further east and the flows to its north and northwest strengthen. The flows into northern Jiangsu Province are cold, and they push further west into Anhui Province, shifting the location of the original convergence zone further west (Figures 7c, 7d, 8c, and 8d). At this time, the surface over-land vortex becomes ill defined. The primary convergence now exists further south behind an east-west oriented gust front that has developed after a cold pool forms underneath the MCS (Figures 8c and 8d). With the establishment of the gust front and through its interaction with low-level flows, the MCS organizes into a bow-shaped echo structure in the second organization stage. During this stage, the circulation of the over-sea vortex also helps enhance the cold pool behind the main gust front by advecting colder air from the northern part of the East China Sea, which further increases the overall cold pool size (cf. Figures 8c, 8d, 12c, and 12d). More quantitive discussion about the impacts of PMCS and its associated cold pool will be present in section 5.

In the second stage, the role of the gust front becomes more dominant, and the strongest convection starts to form at the eastern edge of the cold pool (Figure 8c). The cells surge eastward latter, and eventually creating a bow-shaped echo of high reflectivity by 1500 UTC (Figure 8d). Along the edge of the cold pool that attempts to spread southward, a line of convection is forced and maintained along the gust front, creating a long-tailed, asymmetric bow echo (Figures 5c, 7c, 7d, 8c, and 8d) that shows up on the satellite imagery as a comma-shaped cloud (Figure 3g). The establishment of an organized bow echo helps support a long-duration MCS. Strong surface winds (maximum wind speed reaching ~30 m s^{-1}) are found in a narrow zone behind the gust front at the bow-echo apex in the simulation (not shown). Intense hail-producing convective cells are also found here (Luo et al., 2018; Figure 3g).

4.2. Vertical Structures at CI of HMCS

To help understand the interactions among the convergence line, gust front, as well as the embedded small-scale structures at the times of CI and/or later organization, we examine vertical cross sections of equivalent potential temperature θ_e, water vapor mixing ratio q_v, total condensate water/ice mixing ratio, wind fields, and level of free convection (LFC) (Figure 9). The cross sections are chosen to go through an initiating cell at around 0700 UTC in a plane normal to the low-level convergence line, and at around 1300 UTC roughly perpendicular to the gust front at the later bow echo stage of MCS (as indicated by the blue dashed lines in Figure 7).

For CI in the early stage (left panels of Figure 9 along the cross sections in Figures 7a and 7b), a shallow, more or less symmetric upward moist bulge of high θ_e air is first found at 0600 UTC (Figure 9a). The moist bulge is confined to the lowest 1–2 km within the convergence zone. Such symmetric moisture bulges are typically associated with a zone of low-level wind convergence with minimal temperature contrast and is often the precursor to CI (Wang et al., 2016). The heights of LFC within the moisture bulges are quite low (below 1 km mean sea level [MSL], Figures 9a, 9c, 9e, and 9g). At 0700 UTC, strong uplifting of warm moist air has caused them to reach the LFC and caused liquid condensate to form above 2 km, indicating the initial formation of clouds (indicated by the red contours in Figure 9c). By 0720 UTC, with the presence of moderate to large CAPE, a deep moist convection hence forms reaching above 10 km level. Note that there exist strong downdrafts besides the updrafts in the central of the deep convection at 0720 UTC, which is supposed to be caused by the heavy liquid and ice water loading and hailstone drag effects toward the surface (Figure 9e). Over the next 10 min, the updrafts are stronger, due to enhanced low-level convergence, overcoming the downdrafts caused by the drag effects and creating an upward dent at the tropopause. The hydrometeor content also increases significantly, and the convective storm reaches full intensity. The important role of the low-level convergence during this stage in producing the low-level convergence lifting/forcing is clearly evident.

Quite differently, corresponding to storm organization during the second stage (Figures 7c, 7d, 8c, and 8d), the most distinct features are the establishment of a cold pool during its southeastward propagation (Figures 9b, 9d, 9f, and 9h). The heights of LFC in front of the cold pool are below 2 km MSL, which are favorable for warm air reaching the LFC and conducive to convection initiation at the gust front. Therefore, during the second organization stage, the cold pool and gust front are severe to sharpen the leading edge of the bow-shaped MCS, in terms of temperature and wind (Figures 9d, 9f, and 9h). Besides, the lower LFC heights are considered key elements in trigging new convective storms (Meng et al., 2012; Torri et al., 2015; Trapp & Weisman, 2003; Wang & Xue, 2012).

5. Impacts of PMCS

5.1. Impacts of PMCS on the Evolution of HMCS

As discussed earlier, a proceeding MCS that we call PMCS existed off the Jiangsu-Shandong coast in the prior evening before HMCS was initiated. PMCS moved to be close to the west coast of the Korean Peninsula when initial cells of HMCS were initiated (Figure 2). The initiation and later organization of HMCS were strongly influenced by the low-level circulation. Part of the low-level circulation was from the mesoscale vortex located over the East China Sea that was in the path of PMCS as it moved eastward. The existence of PMCS might have affected the low-level circulation and thereby affected HMCS. To see if this might be true, the circulations at the 3 km and 500 m MSL through much of the life cycle of PMCS are present in Figure 10.

At 2200 UTC 27 April at the 3 km MSL, two main cyclonic circulation centers are found, one near the northwest corner of the plotted domain, and one over the East China Sea off Jiangsu Province extending north to over the Shandong Peninsula (Figure 10a). These two centers should be linked to the two cutoff lows found

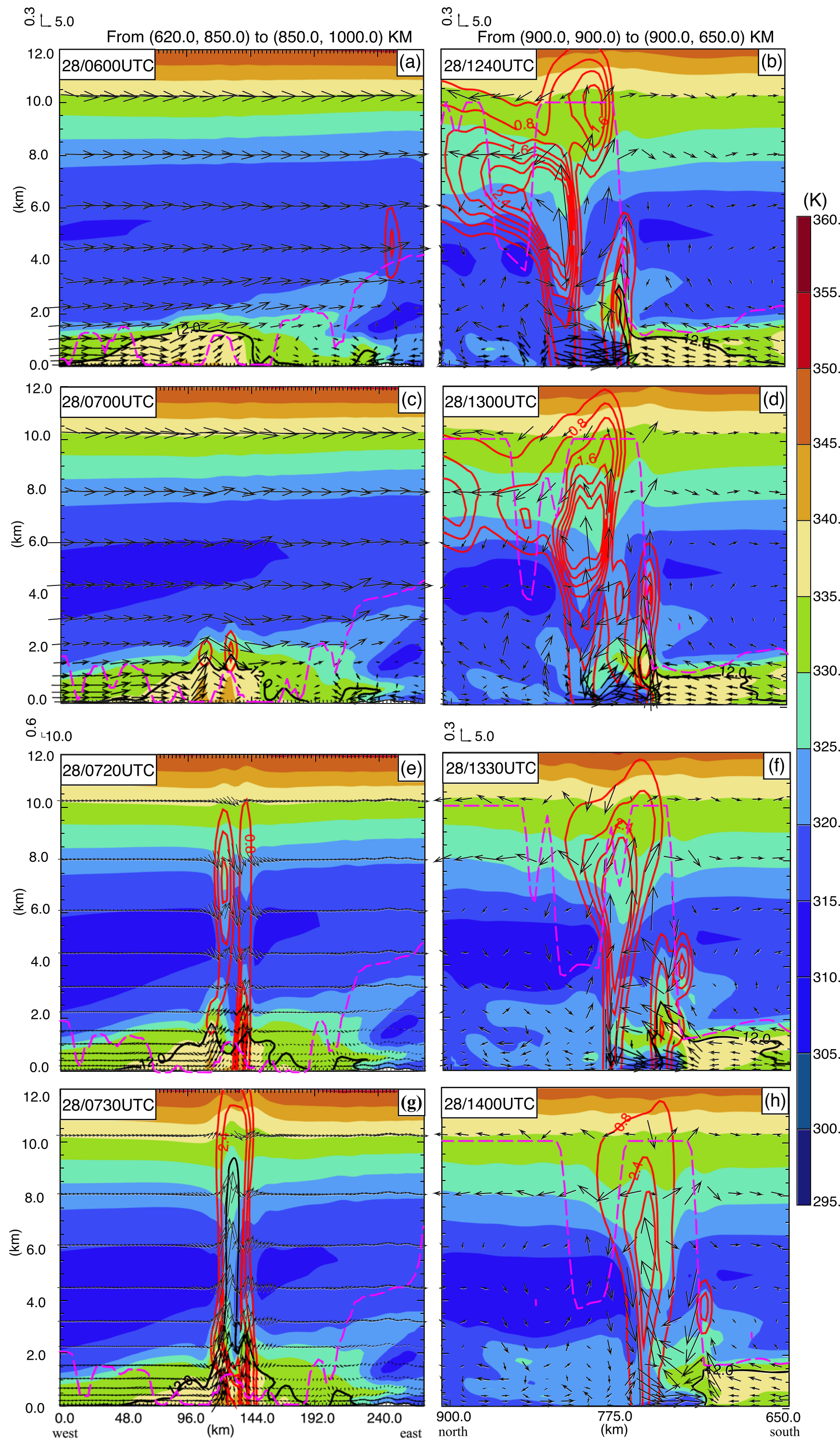

Figure 9. Vertical cross sections of equivalent potential temperature (shaded, K), wind vectors projected to the cross sections (m s^{-1}), and total condensed water/ice mixing ratio (solid red contours, with intervals of 0.8 g kg^{-1}), along the thick blue dashed lines in Figure 7a/7b (left panels: a, c/e, g) and Figure 7d (right panels: b, d, f, h). The solid black contours are for the 12 g kg^{-1} water vapor mixing ratio. The magenta dashed lines denote the corresponding level of free convection (LFC, km) along the cross sections. The magenta dashed lines denote the corresponding level of free convection (LFC, km, MSL) along the cross sections. Note that the reference wind vectors for panels (e) and (g), and their horizontal wind vectors intervals are different from other panels, to give prominence to the vertical wind features within the convective storm.

10.1029/2020JD032606

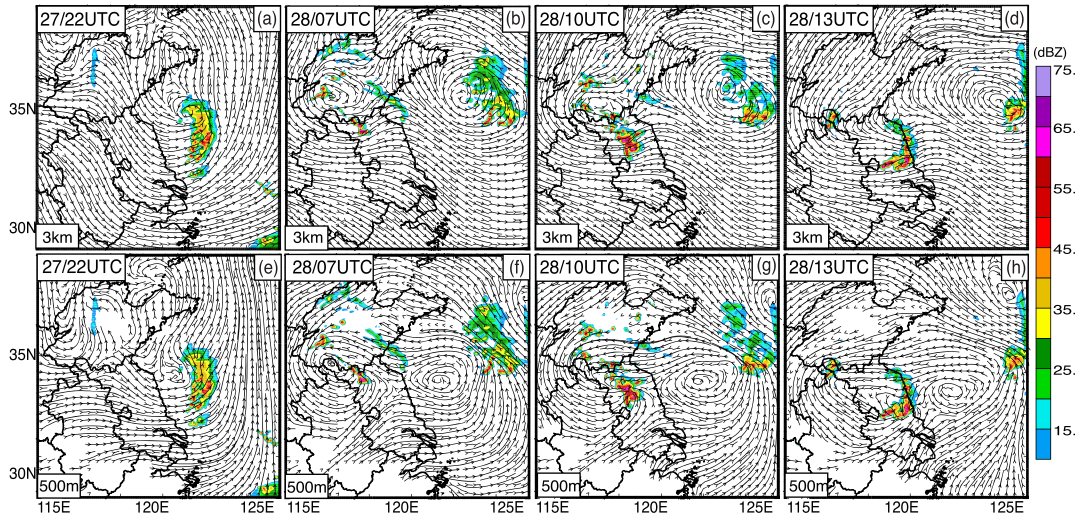

Figure 10. Simulated composite (column-maximum) radar reflectivity (shaded, dBZ) and horizontal wind streamlines at 3 km (a–d) and 500 m MSL (e–h) from control simulation at 2200 UTC 27 April and 0700, 1000, and 1300 UTC 28 April 2015.

at the 500-hPa level (Figure 1a), although the southern part of the East China Sea vortex may have been significantly enhanced by the associated PMCS given the better correspondence in the location of the northern subcenter with the low at the 500-hPa level. At the lower levels, the two subcirculation centers over the sea are more conspicuous (Figure 10e), suggesting a strong effect of PMCS near the surface.

By 0700 UTC 28 April, the western vortex has moved south to over western Shandong Province, and the eastern vortex has organized into a more circular shape with a single center and moves northeastward (Figure 10b). The reflectivity of PMCS is mostly located on the east and southeast side of the vortex center where convergence between easterly flows and southerly flows are strongest. At the 500 m MSL, the western vortex has a good correspondence with that at the 3 km MSL, being located only slightly further south relative to the 3-km location. The eastern vortex center near the surface is located, however, quite far to the southwest of the 3 km center (Figure 10f). The reflectivity of PMCS no long appears to have a strong tie with the eastern surface vortex center at this and later times (Figures 10f–10h).

At 0700 UTC 28 April, new convection initiation occurs at the northern border of Jiangsu Province, at the convergence zone between the southern and northern branches of the western and eastern surface vortices, respectively, as discussed earlier (Figure 10f). Over the next few hours, the evolution of the convection in Jiangsu Province remains strongly controlled by the convergence between the circulations of the two vortices near the surface (Figures 10g and 7b). After 1000 UTC, there are major changes in the organization of convection, with the system evolving from a line of cells moving southeastward into an asymmetric bow-echo MCS, in ways discussed earlier (Figures 10h and 7d). By 1300 UTC, the western vortex center has become less well defined at the surface, and the MCS-induced low-level circulations, for example, those associated with outflow and cold pool, are believed to have contributed to modifying the low-level circulations (Figures 10d and 9h). The eastern surface vortex over the East China Sea, however, does not change much in intensity or location during the period between 0700 and 1300 UTC, almost throughout the life cycle of HMCS (Figures 10f–10h).

The vortices at the 3 km MSL in Figure 10 has close correspondence with the lows on the 500 hPa, which are part of the overall cutoff low circulation. However, the vortices near the surface (lower panels of Figure 10), especially the one over the East China Sea, do not follow closely the 3-km vortices in their movement. The questions we want to ask: What is the origin of the low-level vortex over the East China Sea and what effects PMCS might have on this vortex and on the development and evolution of HMCS, if any? To answer these questions, we design a sensitivity experiment in which PMCS during its early development stage is suppressed. This is done by removing the latent heating and cooling resulting from microphysical processes, mainly from condensation, in the simulation from 1200 UTC 27 April to 0600 UTC 28 April. This corresponds to the so-called "fake dry" option in the WRF model, as was also used in Xue et al. (2018). The

10.1029/2020JD032606

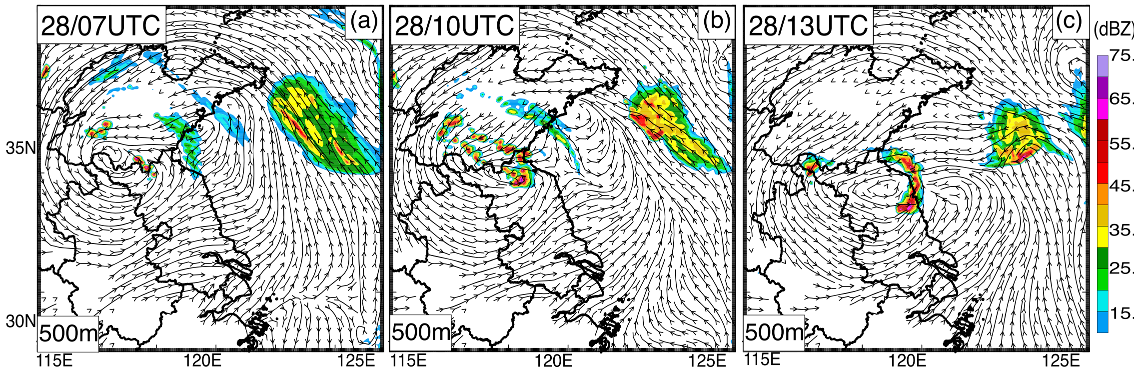

Figure 11. Simulated composite (column-maximum) radar reflectivity (shaded, dBZ) and horizontal wind streamlines 500 m MSL at (a) 0700, (b) 1000, and (c) 1300 UTC 28 April 2015, from the fake-dry sensitivity experiment with PMCS suppressed during its early development period.

condensation and precipitation processes still occur during the simulation, except that the latent heating and cooling are thrown away, so that its heating and cooling effect are off. The differences between the original control and sensitivity experiments can be considered the impacts of PMCS. With the heating and cooling effect turned off, the development of PMCS during the period is suppressed, although the system does develop later on when heating and cooling are turned back on due to the presence of abundant convective instability. The MCS developed later does not produce features such as the low-level cold pool and associated circulation as in the original control run during the early period.

The streamlines and composite radar reflectivity at 500 m MSL within the sensitivity experiment at 0700, 1000, and 1300 UTC 28 April are shown in Figure 11. It is seen that with the early stage development of PMCS suppressed, the prominent low-level cyclonic vortex over the East China Sea, as shown in Figures 10f–10h, does not form (Figure 11). The MCS does still develop over the sea after latent heating and cooling are turned on from 0600 UTC in the sensitivity simulation, it is, however, rather different from that in the control experiment, in terms of its location and structure (compare Figures 11a–11c with Figures 10f–10h). The MCS that develops over Jiangsu Province also behaves very differently; the convective cells are initiated in northern Jiangsu Province (Figures 11a and 11b), at somewhat eastward locations than in the control experiment (cf. Figures 7a and 7b). Also, by 1300 UTC, the main convective system organizes into an eastward propagating convective line over the northern Jiangsu Province and moves into the East China Sea (Figure 11c), instead of sweeping southeastward through most of Jiangsu Province as in the control experiment (Figures 10f–10h) and in reality (Figure 5). Clearly, the evolution of the MCS over Jiangsu is very different in the two experiments.

5.2. Rearward Spreading Cold Pool Induced by PMCS

To gain more insights on the impacts of PMCS, the difference (control minus sensitivity) fields of 500 m MSL potential temperature and wind during the life of PMCS are shown in Figure 12. The potential temperature difference reveals the differences in the low-level cold pools associated with PMCS and HMCS in the control and fake-dry runs. The cold pool over the East China Sea is more than 7 K colder than that in the fake-dry run at 2200 UTC 27 April (Figure 12a), and the difference is maintained through 1300 UTC 28 April although the difference has become smaller (Figure 12d). Over the East China Sea, the prevailing low-level flow is easterly, so that the cold pool associated with PMCS is mostly spreading westward toward the eastern coast of China. The potential temperature differences over Jiangsu Province at 1300 UTC 28 April (Figure 12d) are due to the evaporation and melting of precipitation hydrometeors including hail from HMCS in the control simulation. The most prominent features in the low-level flow difference are the cyclonic and anticyclonic circulations located respectively on the south and north of the maximum temperature difference (or cold pool) starting from 2200 UTC (Figure 12a). The cyclonic and anticyclonic circulations increase in size with time (Figures 12b and 12d), and the circulations are also consistent with the westward spreading cold pool, where circulations of opposite signs develop on its south and north flanks.

West–east vertical cross sections at the respective location of strongest westward cold pool outflow (along red dashed lines in Figure 12) are plotted in Figure 13. They show that the air above 3 km MSL level is

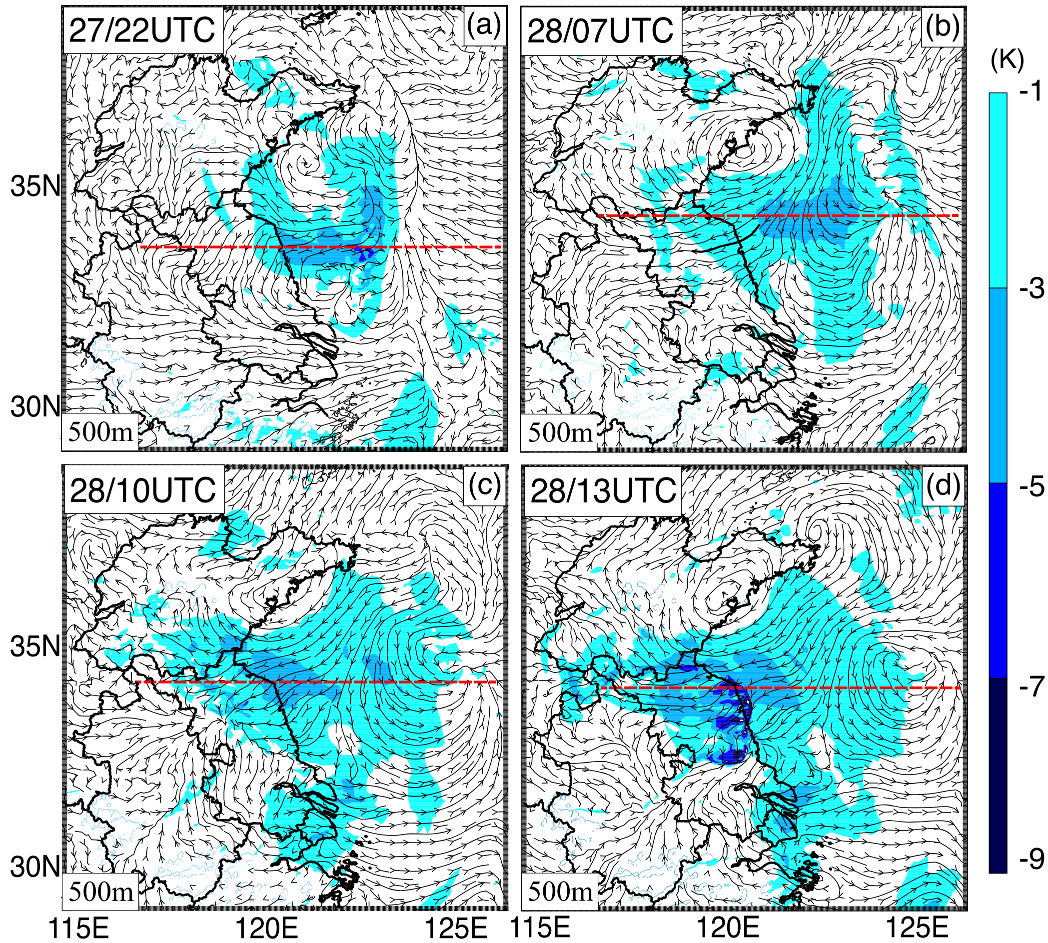

Figure 12. Potential temperature (shaded, K) and horizontal wind (wind streamlines) difference (control experiment minus fake-dry sensitivity experiment) at 500 m MSL at (a) 2200 UTC 27 April and (b) 0700, (c) 1000, and (d) 1300 UTC 28 April. The dashed red lines denote the locations of cross sections in Figure 13.

significantly warmer in control, due to latent heating from PMCS, and the air below 3 km MSL is colder due to evaporative cooling. A wedge-shaped cold pool is mostly confined below 1 km MSL, and its leading edge or the gust front is located at around 118.5°E horizontal coordinate at 2200 UTC 27 April (Figure 13a). This gust front (if defined in terms of the potential temperature deficit between the two runs, which roughly matches the leading edge of the easterly difference winds) advances further westward toward the east coast of Jiangsu Province by 1300 UTC 28 April (Figure 13d).

5.3. Genesis of the Cyclonic Mesoscale Vortice Over the East China Sea

Above the shallow cold pool outflow are strong westerly flows, creating large horizontal vorticity between the two flow layers, with the vorticity pointing northward into the plotting plane in Figure 13. Correspondingly, rotor circulations are clearly evident in the vertical cross sections, especially at ~900 km in Figures 13b and 13c. Such circulation structures are consistent with the prediction by the RKW theory (Rotunno et al., 1988), given the eastward shear of the flows ahead of the gust front. Such a setup is unfavorable for triggering convection at the gust front, until the outflow (together with the background circulation) meets stronger opposing flows with more favorable near-surface vertical shear (cf. left panels of Figure 9). This occurs near the northwest corner of Jiangsu Province (cf. Figures 7a and 7b) where the westerly winds of the surface vortex over land converge with the easterly winds on the northwestern side of the East China Sea vortex (Figure 7a).

The horizontal vortex tube, defined as the surface in the continuum formed by all vortex lines passing through a closed curve in the continuum (Vallis, 2006), associated with the rotor circulations as seen in

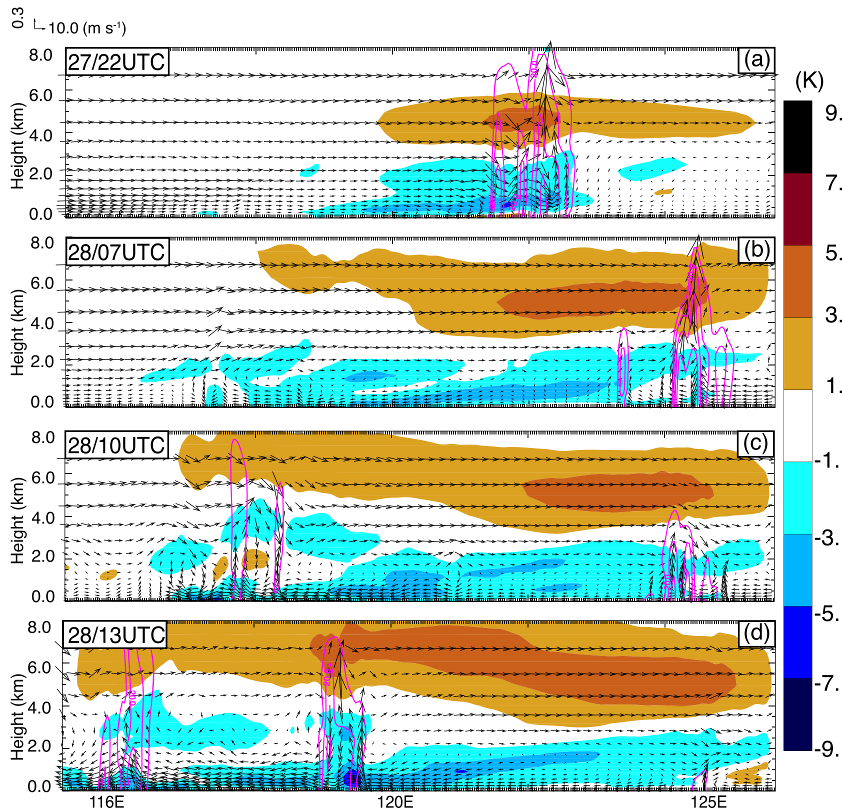

Figure 13. (a–d) Vertical cross sections of potential temperature difference (shaded, K) and the wind vectors difference (control experiment minus fake-dry sensitivity experiment) along the red dashed lines in Figure 12. The magenta contours are for radar reflectivity at intervals of 10 dBZ from the control experiment, and such reflectivity contours are associated with PMCS and newly initialized HMCS.

Figure 13, are results of baroclinic vorticity generation at the leading edge of the cold pool or gust front where horizontal buoyancy gradient exists. Vortex tubes are generally nested around the axis of rotation, and such vorticity is advected along the cold pool—environmental flow interface to the rear (eastward in this case) of the gust front (Rotunno et al., 1988; Xue et al., 1997). Some of the horizontal vorticity also comes from the shear of environmental flow (westerly flow going over the cold pool). The convergence between the westward spreading cold pool and the westerly flows at the gust front is the strongest at the western edge of the gust front and creates enhanced lifting at the apex of the bow-shaped gust front. Thus, the horizontal vortex that had developed along the gust front is lifted more than on its southern and northern sides, causing the upward tilting of the vortex tube, and resulting an arc shaped vortex tube. The result of such vortex tube arching is the couplet of mesoscale vortices on the northern and southern sides of the cold pool. The couplet cyclonic and anticyclonic circulations are superimposed on top of the background cyclonic circulation at the larger scale (as seen in Figure 11, which can be viewed as the background circulation unaffected by the cold-pool-induced circulations). As a result, the southern cyclonic circulation is enhanced while the northern anticyclonic circulation is mostly canceled out by the background circulation, leading to the dominant cyclonic circulation or vortex over the East China Sea (see lower panels of Figure 10). In another word, adding the flow in Figure 12b to that of Figure 11a results in the flow in Figure 10f. The vortex over land is not much affected by PMCS cold pool and is similar with and without the initial PMCS (compare Figures 11a and 10f). The vortices over land and over the sea set up a convergence zone on the east side of the overland vortex center to trigger convection (Figures 7a, 7b, and 10f), and the southwestern flows supply moist unstable air (Figure 2d) to feed triggered convection.

The formation of vortex couplet at the gust front due to the tilting and arching of baroclinically generated horizontal vortex tube along the gust front has been discussed in several studies in various context (Atkins et al., 2004; Marquis et al., 2008; Schenkman et al., 2012; Wakimoto, Murphey, Davis, et al., 2006; Wakimoto, Murphey, Nester, et al., 2006). For example, similar to the vortex couplet genesis mechanism

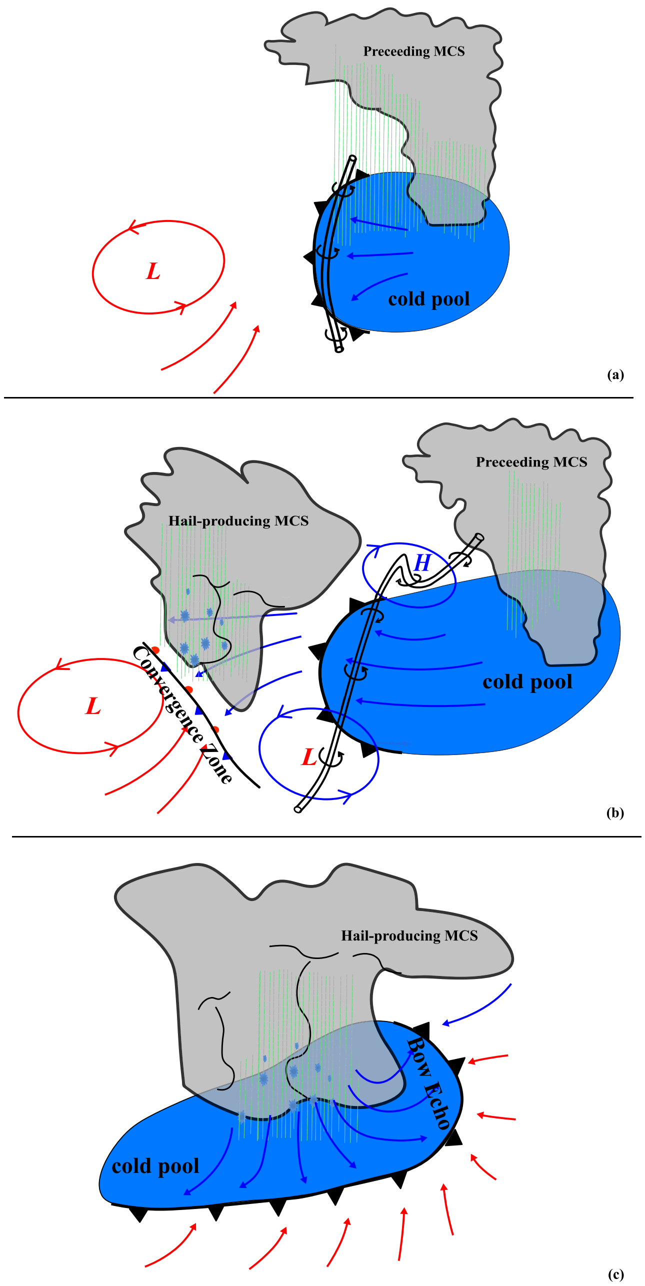

Figure 14. (a–c) Conceptual model for the initiation and organization of a long-lasting multicellular hail-producing MCS following a preceding MCS to its east. A vortex tube is drawn in (a) and (b) whose sense of rotation is indicated by arrowed rings around the tube. Surface vortex circulations are drawn as red and blue arrowed circuits, and cold pool is shaded blue. Gust front is drawn like traditional cold front. Representative flows are indicated by curved arrows of different colors.

within this study, Atkins and Laurent (2009) propose that the vortex couplet within intense bow echo is produced by the upward tilting of baroclinically generated vortex lines at the gust front based on quasi-idealized simulations of an observed bow echo event. In Schenkman et al. (2012), similar processes are found where the arching of a vortex tube is attributed to be the main source of mesovortex rotation near a bowing segment of a gust front in a real MCS case. A similar concept model was proposed earlier by Trapp and Weisman (2003). In all these studies, the eastward spreading cold pool creates a couplet of circulations with the cyclonic one located on the north side. Somewhat different from the above is the tilting of horizontal vortex tubes downward by the downdraft, resulting in couplet circulations of opposite signs on the north and south sides (Trapp & Weisman, 2003; Wakimoto, Murphey, Davis, et al., 2006). As reviewed in Schenkman and Xue (2016), the above papers deal with the generation and sources of vorticity of much smaller meso-γ scale mesovortices in bow echoes or quasi-linear convective systems. While in this paper, the vortices are of mesoscale and are associated with a larger and weaker cold pool that spreads on the "back side" toward the rear of an MCS. The isolation and identification of the MCS cold-pool-induced circulations from the background and discussions on their roles in triggering and organizing subsequent convection and MCS are novel aspects of this study. We are not aware of any other study taking the same approach.

6. A Conceptual Model for a Long-Lasting Multicellular Hail-Producing MCS

Based on the analyses, a three-stage conceptual model is proposed in Figure 14, summarizing the initiation and organization of HMCS within this study.

Before the development of the main over-land MCS, precipitation from a proceeding MCS generates a cold pool off the eastern China coast over the Eastern China Sea (Figure 14a).

Horizontal convergence and localized upward motion produced at the gust front by the outflow of the rearward/westward spreading cold pool act to tilt and stretch baroclinically horizontal vorticity, creating a couplet of mesoscale vortices on the south and north side of the cold pool (Figure 14b). Combined with the background cyclonic circulation, the southern cyclonic vortex becomes the most prominent low-level feature over the East China Sea. At this time, another mesoscale low-level vortex exists over land that is associated with a small cutoff low at 500 hPa. Between the southwesterly flows on the southeast side of the overland vortex and the northeasterly winds on the northwest side of the over-ocean vortex is a strong convergence zone along which initial convective cells are triggered and subsequently intensified. On the southwest side of the convergence zone are moist southwesterly flows with moderately large CAPE, providing fuel to the organization of a long-lasting hail-producing MCS (Figure 14b).

After the initiation, the storms organize into a northwest-southeast line and move southeastward. A cold pool is established underneath the MCS, which aided by cold advection from the East China Sea. The cold pool accelerates the southward and southeastward propagation of the MCS, establishing a west-east orientation along the gust front and later the development of eastward protruding bow at the east end of the convective line (Figure 14c).

7. Summary and Conclusions

This study examines the initiation and organization of a long-lasting (for about 7 hr) hail-producing MCS (referred as HMCS) that swept north-south across most of Jiangsu Province in Eastern China on 28 April 2015. Synoptic-scale analyses indicate that the storm environment was characterized by a deep semi-permanent East Asia trough over Eastern China, in which two small cutoff lows existed within a deep low at the 500-hPa level. Corresponding to these two cutoff lows are two mesoscale cyclonic circulations or vortex centers at the 850-hPa level and at the surface, one over the land northwest of Jiangsu Province and one over the East China Sea, although the latter was significantly enhanced by a proceeding MCS (referred as PMCS). The strong low-level convergence and moderately high CAPE over Jiangsu Province make the overall environment conducive to the development of MCS.

The life cycles of HMCS and PMCS were simulated successfully by the ARPS model using a 3-km grid spacing and a three-moment microphysics scheme. Comparisons with radar observations show that the model simulation reproduces reasonably well the general evolution of HMCS. For example, the model reproduces well the initiation and intensification of initial convective cells near the northwest border of Jiangsu Province, their subsequent organization into an MCS and eventual development of a bow-shaped echo at the eastern portion of the MCS. The model also produces a swath of surface accumulated precipitation that is close to the observation, except for certain overestimation of the peak precipitation.

To further examine the initiation and organization processes of HMCS, a fake-dry simulation is conducted, in which latent heating and cooling effects are disabled during the earlier development period of PMCS before the initiation of HMCS. Based on the results of both control and fake-dry simulations, the convective initiation and subsequent organization into HMCS are investigated, with particular attention paid to the linkage between HMCS and PMCS that moves into the East China Sea. The near-surface differences in wind and temperature fields between the fake-dry and control simulations show a mesoscale cold pool underneath PMCS, spreading westward toward the eastern coast of China, due to effective cooling from PMCS. Baroclinically generated horizontal vortex tube along the leading edge of the cool pool or gust front is tilted upward at the central portion, forming a vortex tube arch. At the southern end of the arch is a cyclonic circulation center while at the northern end is an anticyclonic center. The coupling of two centers and the broad cyclonic circulation underneath the upper-level low results in an enhanced mesoscale cyclonic vortex over the East China Sea while the northern anticyclone is mostly canceled out by the background cyclonic circulation. It is the establishment of this intense cyclonic vortex off the coast of Jiangsu Province that creates enhanced near-surface convergence with the circulation of over-land vortex. The near-surface convergence triggers initial convection in northwestern Jiangsu and affects subsequent organization of HMCS. The development and evolution of HMCS in the fake-dry simulation are quite different from that in the control simulation. In the fake-dry simulation, the initial cells are triggered somewhat further east, and HMCS takes a more northerly path and moves eastward instead of southeastward later on as in reality. A three-stage conceptual model has been proposed to summarize the initiation and organization for HMCS.

In general, it is noted that although the conceptual model proposed in this study is based on a single case only, the understanding of the complex interactions between two MCSs leading to severe weather should be valuable to operational forecasters when encountering similar situations. Quantitative vorticity budget analyses for the parcels around the rearward spreading cold pool can be performed to further support our conclusions, although we believe the physical mechanisms proposed herein should be robust. There are many studies on convective initiation along outflow boundaries of prior precipitation systems, but we are not aware of studies documenting the sequence of processes identified in this study. The frequency of such events actually in eastern China region will require future climatological studies.

Data Availability Statement

NCEP 1° GFS final analysis data can be downloaded freely online (http://rda.ucar.edu/datasets/ds083.2/). The FY-2E satellite data set can be downloaded online (http://satellite.nsmc.org.cn/portalsite/default.aspx?currentculture=en-US), and the radar data set is provided by the Climate Data Center at National Meteorological Information Center of China Meteorology Administration. The processed data sets within this paper, including the radar, satellite, surface precipitation, and NCEP 1° GFS final analysis datasets are available online (https://doi.org/10.7910/DVN/8P16YK).

Acknowledgments
This work was primarily supported by the Ministry of Science and Technology of the People's Republic of China (MOST) (2018YFC1507303), by NSFC Grants 41730965, 419505044, and 41975124, by the Fundamental Research Funds for the Central Universities of China (2019B00614), and Jiangsu Province Entrepreneurship and Innovation Plan (B19164). Liping Luo was supported by Nanjing University for her extended visit at the Center for Analysis and Prediction of Storms, University of Oklahoma. Suggestions and comments from Bowen Zhou improved our paper.

References

Adler, B., Kalthoff, N., & Gantner, L. (2011). The impact of soil moisture inhomogeneities on the modification of a mesoscale convective system: An idealised model study. *Atmospheric Research*, *101*(1-2), 354–372. https://doi.org/10.1016/j.atmosres.2011.03.013

Atkins, N. T., Arnott, J. M., Przybylinski, R. W., Wolf, R. A., & Ketcham, B. D. (2004). Vortex structure and evolution within bow echoes. Part I: Single-Doppler and damage analysis of the 29 June 1998 derecho. *Monthly Weather Review*, *9*, 10,275–10,286.

Atkins, N. T., & Laurent, M. S. (2009). Bow echo mesovortices. Part II: Their genesis. *Monthly Weather Review*, *137*(5), 1514–1532. https://doi.org/10.1175/2008MWR2650.1

Bai, L., Meng, Z., Huang, Y., Zhang, Y., Niu, S., & Su, T. (2019). Convection initiation resulting from the interaction between a quasi-stationary dryline and intersecting gust fronts: A case study. *Journal of Geophysical Research: Atmospheres*, *124*, 2379–2396. https://doi.org/10.1029/2018JD029832

Barthlott, C., Schipper, J. W., Kalthoff, N., Adler, B., Kottmeier, C., Blyth, A., & Mobbs, S. (2010). Model representation of boundary-layer convergence triggering deep convection over complex terrain: A case study from COPS. *Atmospheric Research*, *95*(2-3), 172–185. https://doi.org/10.1016/j.atmosres.2009.09.010

Browning, K. A., Blyth, A., Clark, P., Corsmeier, U., Morcrette, C., Agnew, J., et al. (2007). The convective storm initiation project. *Bull. Amer. Meteor. Soc.*, *88*, 1939–1956. https://doi.org/10.1175/BAMS-88-12-1939

Cai, H., Lee, W. C., Weckwerth, T. M., Flamant, C., & Murphey, H. V. (2010). Observations of the 11 June dryline during IHOP_2002—A null case for convection initiation. *Monthly Weather Review*, *134*, 336–354.

Chen, X., Liu, X., Li, X., Liu, M., & Yang, M. (2018). Activity characteristics of the East Asian trough in CMIP5 models. *Atmosphere*, *9*(2), 67. https://doi.org/10.3390/atmos9020067

Corfidi, S. F., Corfidi, S. J., & Schultz, D. M. (2008). Elevated convection and castellanus: Ambiguities, significance, and questions. *Weather and Forecasting*, *23*(6), 1280–1303. https://doi.org/10.1175/2008WAF2222118.1

Costa, S., Mezzasalma, P., Levizzani, V., Alberoni, P. P., & Nanni, S. (2001). Deep convection over Northern Italy: Synoptic and thermodynamic analysis. *Atmospheric Research*, *56*(1-4), 73–88. https://doi.org/10.1016/S0169-8095(00)00091-0

Duffourg, F., Nuissier, O., Ducrocq, V., Flamant, C., Chazette, P., Delanoë, J., et al. (2016). Offshore deep convection initiation and maintenance during I0P16a Offshore deep convection initiation and maintenance during HyMeX IOP 16a heavy precipitation event. *Quarterly Journal of the Royal Meteorological Society*, *142*, 259–274. https://doi.org/10.1002/qj.2725

Fabry, F. (2006). The spatial variability of moisture in the boundary layer and its effect on convection initiation: Project-long characterization. *Monthly Weather Review*, *134*(1), 79–91. https://doi.org/10.1175/MWR3055.1

Feng, Y., & Zhao, X. (2015). Changes in spatiotemporal pattern of precipitation over China during 1980–2012. *Environment and Earth Science*, *73*(4), 1649–1662. https://doi.org/10.1007/s12665-014-3517-x

Fortin, V., Therrien, C., & Anctil, F. (2008). Correcting wind-induced bias in solid precipitation measurements in case of limited and uncertain data. *Hydrological Processes*, *22*(17), 3393–3402. https://doi.org/10.1002/hyp.6959

Frye, J. D., & Mote, T. L. (2010). Convection initiation along soil moisture boundaries in the southern Great Plains. *Monthly Weather Review*, *138*(4), 1140–1151. https://doi.org/10.1175/2009MWR2865.1

Geerts, B., Parsons, D., Ziegler, C. L., Weckwerth, T. M., Biggerstaff, M. I., Clark, R. D., et al. (2017). The 2015 plains elevated convection at night field project. *Bulletin of the American Meteorological Society*, *98*(4), 767–786. https://doi.org/10.1175/BAMS-D-15-00257.1

Gerken, T., Bromley, G. T., & Stoy, P. C. (2018). Surface moistening trends in the northern North American Great Plains increase the likelihood of convective initiation. *Journal of Hydrometeorology*, *19*(1), 227–244. https://doi.org/10.1175/JHM-D-17-0117.1

Grilli, S. T., O'Reilly, C., Harris, J. C., Bakhsh, T. T., Tehranirad, B., Banihashemi, S., et al. (2015). Modeling of SMF tsunami hazard along the upper US East Coast: Detailed impact around ocean city, MD. *Natural Hazards*, *76*(2), 705–746. https://doi.org/10.1007/s11069-014-1522-8

Hu, K. X., Lu, R., & Wang, D. H. (2010). Seasonal climatology of cut-off lows and associated precipitation patterns over Northeast China. *Meteorology and Atmospheric Physics*, *106*(1-2), 37–48. https://doi.org/10.1007/s00703-009-0049-0

Huang, Y., Meng, Z., Li, J., Li, W., Bai, L., Zhang, M., & Wang, X. (2017). Distribution and variability of satellite-derived signals of isolated convection initiation events over central Eastern China. *Journal of Geophysical Research: Atmospheres*, *122*, 11,357–11,373. https://doi.org/10.1002/2017JD026946

Knippertz, P., & Martin, J. E. (2007). The role of dynamic and diabatic processes in the generation of cut-off lows over Northwest Africa. *Meteorology and Atmospheric Physics*, *96*(1-2), 3–19. https://doi.org/10.1007/s00703-006-0217-4

Koukoula, M., Nikolopoulos, E. I., Kushta, J., Bartsotas, N. S., Kallos, G., & Anagnostou, E. N. (2019). A numerical sensitivity analysis of soil moisture feedback on convective precipitation. *Journal of Hydrometeorology*, *20*(1), 23–44. https://doi.org/10.1175/JHM-D-18-0134.1

Lean, H. W., Roberts, N. M., Peter, A. C., & Cyril, M. (2009). The surprising role of orography in the initiation of an isolated thunderstorm in Southern England. *Monthly Weather Review*, *137*(9), 3026–3046. https://doi.org/10.1175/2009MWR2743.1

Lee, K. O., Flamant, C., Ducrocq, V., Duffourg, F., Fourrié, N., & Davolio, S. (2016). Convective initiation and maintenance processes of two back-building mesoscale convective. *Quarterly Journal of the Royal Meteorological Society*, *142*(700), 2623–2635. https://doi.org/10.1002/qj.2851

Li, D., Sun, J., Fu, S., Wei, J., Wang, S., & Tian, F. (2016). Spatiotemporal characteristics of hourly precipitation over central eastern China during the warm season of 1982–2012. *International Journal of Climatology*, *36*(8), 3148–3160. https://doi.org/10.1002/joc.4543

Lian, Y., Shen, B., Li, S., Liu, G., & Yang, X. (2016). Mechanisms for the formation of Northeast China cold vortex and its activities and impacts: An overview. *Journal of Marine Research*, *30*(6), 881–896. https://doi.org/10.1007/s13351-016-6003-4

Liu, H., & Xue, M. (2008). Prediction of convective initiation and storm evolution on 12 June 2002 during IHOP_2002. Part I: Control simulation and sensitivity experiments. *Monthly Weather Review*, *136*(7), 2261–2282. https://doi.org/10.1175/2007MWR2161.1

Luo, L., Xue, M., Zhu, K., & Zhou, B. (2017). Explicit prediction of hail using multimoment microphysics schemes for a hailstorm of 19 March 2014 in eastern China. *Journal of Geophysical Research: Atmospheres*, *122*, 7560–7581. https://doi.org/10.1002/2017JD026747

Luo, L., Xue, M., Zhu, K., & Zhou, B. (2018). Explicit prediction of hail in a long-lasting multicellular convective system in Eastern China using multimoment microphysics schemes. *Journal of the Atmospheric Sciences*, *75*(9), 3115–3137. https://doi.org/10.1175/JAS-D-17-0302.1

Luo, Y., Gong, Y., & Zhang, D.-L. (2014). Initiation and organizational modes of an extreme-rain-producing mesoscale convective system along a Mei-Yu front in East China. *Monthly Weather Review*, *142*(1), 203–221. https://doi.org/10.1175/MWR-D-13-00111.1

Luo, Y., Wang, H., Zhang, R., Qian, W., & Luo, Z. (2013). Comparison of rainfall characteristics and convective properties of monsoon precipitation systems over South China and the Yangtze and Huai River Basin. *Journal of Climate*, *26*(1), 110–132. https://doi.org/10.1175/JCLI-D-12-00100.1

Marquis, J., Richardson, Y., Wurman, J., & Markowski, P. (2008). Single- and dual-Doppler analysis of a tornadic vortex and surrounding storm-scale flow in the Crowell, Texas, supercell of 30 April 2000. *Monthly Weather Review*, *136*(12), 5017–5043. https://doi.org/10.1175/2008MWR2442.1

Marsham, J. H., Trier, S. B., Weckwerth, T. M., & Wilson, J. W. (2011). Observations of elevated convection initiation leading to a surface-based squall line during 13 June IHOP_2002. *Monthly Weather Review*, *139*(1), 247–271. https://doi.org/10.1175/2010MWR3422.1

Maurer, V., Bischoff-Gauß, I., Kalthoff, N., Gantner, L., Roca, R., & Panitz, H. J. (2017). Initiation of deep convection in the Sahel in a convection-permitting climate simulation for northern Africa. *Quarterly Journal of the Royal Meteorological Society*, *143*(703), 806–816. https://doi.org/10.1002/qj.2966

Meng, Z., Zhang, F., Markowski, P., Wu, D., & Zhao, K. (2012). A modeling study on the development of a bowing structure and associated rear inflow within a squall line over South China. *Journal of the Atmospheric Sciences*, *69*(4), 1182–1207. https://doi.org/10.1175/JAS-D-11-0121.1

Milbrandt, J., & Yau, M. (2005). A multimoment bulk microphysics parameterization. Part II: A proposed three-moment closure and scheme description. *Journal of the Atmospheric Sciences*, *62*(9), 3065–3081. https://doi.org/10.1175/JAS3535.1

Molini, A., Lanza, L. G., & La Barbera, P. (2005). The impact of tipping-bucket rain gauge measurement errors on design rainfall for urban-scale applications. *Hydrological Processes*, *19*(5), 1073–1088. https://doi.org/10.1002/hyp.5646

Parsons, D. B., Haghi, R. K., Halbert, T., Elmer, B., & Wang, J. (2019). The potential role of atmospheric bores and gravity waves in the initiation and maintenance of nocturnal convection over the Southern Great Plains. *Journal of the Atmospheric Sciences*, *76*(1), 43–68. https://doi.org/10.1175/JAS-D-17-0172.1

Pleim, J. E., & Xiu, A. (1995). Development and testing of a surface flux and planetary boundary layer model for application in mesoscale models. *Journal of Applied Meteorology*, *34*(1), 16–32. https://doi.org/10.1175/1520-0450-34.1.16

Rasmussen, K. L., & Houze, R. A. (2016). Convective initiation near the Andes in Subtropical South America. *Monthly Weather Review*, *144*(6), 2351–2374. https://doi.org/10.1175/MWR-D-15-0058.1

Reif, D. W., & Bluestein, H. B. (2018). Initiation mechanisms of nocturnal convection without nearby surface boundaries over the Central and Southern Great Plains during the warm season. *Monthly Weather Review*, *146*(9), 3053–3078. https://doi.org/10.1175/MWR-D-18-0040.1

Rotunno, R., Klemp, J. B., & Weisman, M. L. (1988). A theory for strong, long-lived squall lines. *Journal of the Atmospheric Sciences*, *45*(3), 463–485. https://doi.org/10.1175/1520-0469(1988)045<0463:ATFSLL>2.0.CO;2

Schenkman, A. D., & Xue, M. (2016). Bow-echo mesovortices: A review. *Atmospheric Research*, *170*, 1–13. https://doi.org/10.1016/j.atmosres.2015.11.003

Schenkman, A. D., Xue, M., & Shapiro, A. (2012). Tornadogenesis in a simulated mesovortex within a mesoscale convective system. *Journal of the Atmospheric Sciences*, *69*(11), 3372–3390. https://doi.org/10.1175/JAS-D-12-038.1

Shen, Y., Zhao, P., Pan, Y., & Yu, J. (2014). A high spatiotemporal gauge-satellite merged precipitation analysis over China. *Journal of Geophysical Research: Atmospheres*, *119*, 3063–3075. https://doi.org/10.1002/2013JD020686

Song, L., Wang, L., Chen, W., & Zhang, Y. (2016). Intraseasonal variation of the strength of the East Asian trough and its climatic impacts in boreal winter. *Journal of Climate*, *29*(7), 2557–2577. https://doi.org/10.1175/JCLI-D-14-00834.1

Su, T., & Zhai, G. (2016). The role of convectively generated gravity waves on convective initiation: A case study. *Monthly Weather Review*, *145*, 335–359.

Sun, W., & Chang, C. (1986). Diffusion model for a convective layer. Part I: Numerical simulation of convective boundary layer. *Journal of Applied Meteorology*, *25*(10), 1445–1453. https://doi.org/10.1175/1520-0450(1986)025<1445:DMFACL>2.0.CO;2

Taylor, C. M., & Ellis, R. J. (2006). Satellite detection of soil moisture impacts on convection at the mesoscale. *Geophysical Research Letters*, *33*, L03404. https://doi.org/10.1029/2005GL025252

Taylor, C. M., Gounou, A., Guichard, F., Harris, P. P., Ellis, R. J., Couvreux, F., & De Kauwe, M. (2011). Frequency of Sahelian storm initiation enhanced over mesoscale soil-moisture patterns. *Nature Geoscience*, *4*(7), 430–433. https://doi.org/10.1038/ngeo1173

Taylor, C. M., Parker, D. J., Kalthoff, N., Gaertner, M. A., Philippon, N., Bastin, S., et al. (2011). New perspectives on land–atmosphere feedbacks from the African Monsoon Multidisciplinary Analysis. *Atmospheric Science Letters*, *12*(1), 38–44. https://doi.org/10.1002/asl.336

Torri, G., Kuang, Z., & Tian, Y. (2015). Mechanisms for convection triggering by cold pools. *Geophysical Research Letters*, *42*, 1943–1950. https://doi.org/10.1002/2015GL063227

Trapp, R. J., & Weisman, M. L. (2003). Low-level mesovortices within squall lines and bow echoes. Part II: Their genesis and implications. *Monthly Weather Review*, *131*(11), 2804–2823. https://doi.org/10.1175/1520-0493(2003)131<2804:LMWSLA>2.0.CO;2

Trier, S. B., Chen, F., & Manning, K. W. (2004). A study of convection initiation in a mesoscale model using high-resolution land surface initial conditions. *Monthly Weather Review*, *132*, 298–302. https://doi.org/10.1175/MWR2839.1

Tsai, Y. M., Kuo, H. C., & Schubert, W. H. (2010). Filamentation time diagnosis of thinning troughs and cutoff lows. *Monthly Weather Review*, *138*(6), 2327–2335. https://doi.org/10.1175/2010MWR3102.1

Vallis, G. K. (2006). *Atmospheric and oceanic fluid dynamics* (p. 745). Cambridge, UK: Cambridge University Press.

Wakimoto, R. M., Murphey, H. V., Davis, C. A., & Atkins, N. T. (2006). High winds generated by bow echoes. Part II: The relationship between the mesovortices and damaging straight-line winds. *Monthly Weather Review*, *134*(10), 2813–2829. https://doi.org/10.1175/MWR3216.1

Wakimoto, R. M., Murphey, H. V., Nester, A., Jorgensen, D. P., & Atkins, N. T. (2006). High winds generated by bow echoes. Part I: Overview of the Omaha bow echo 5 July 2003 storm during BAMEX. *Monthly Weather Review*, *134*(10), 2793–2812. https://doi.org/10.1175/MWR3215.1

Walker, J. R., Mackenzie, W. M. Jr., Mecikalski, J. R., & Jewett, C. P. (2012). An enhanced geostationary satellite-based convective initiation algorithm for 0-2-h nowcasting with object tracking. *Journal of Applied Meteorology and Climatology*, *51*(11), 1931–1949. https://doi.org/10.1175/JAMC-D-11-0246.1

Wang, H., Luo, Y., & Jou, B. J.-D. (2014). Initiation, maintenance, and properties of convection in an extreme rainfall event during SCMREX: Observational analysis. *Journal of Geophysical Research: Atmospheres*, *119*, 13,206–13,232. https://doi.org/10.1002/2014JD022339

Wang, L., Chen, W., Zhou, W., & Huang, R. (2009). Interannual variations of East Asian Trough axis at 500 hPa and its association with the East Asian winter monsoon pathway. *Journal of Climate*, *22*(3), 600–614. https://doi.org/10.1175/2008JCLI2295.1

Wang, Q., Xue, M., & Tan, Z. (2016). Convective initiation by topographically induced convergence forcing over the Dabie Mountains on 24 June 2010. *Advances in Atmospheric Sciences*, *33*(10), 1120–1136. https://doi.org/10.1007/s00376-016-6024-z

Wang, Q. W., & Xue, M. (2012). Convective initiation on 19 June 2002 during IHOP: High-resolution simulations and analysis of the mesoscale structures and convection initiation. *Journal of Geophysical Research*, *117*, D12107. https://doi.org/10.1029/2012JD017552

Wang, Q. W., & Xue, M. (2018). A high-resolution modeling study of the 19 June 2002 convective initiation case during IHOP_2002: Localized forcing by horizontal convective rolls. *Advances in Atmospheric Sciences*, *35*(10), 1243–1253. https://doi.org/10.1007/s00376-018-7218-3

Weckwerth, T. M., & Parsons, D. B. (2006). A review of convection initiation and motivation for IHOP_2002. *Monthly Weather Review*, *134*(1), 5–22. https://doi.org/10.1175/MWR3067.1

Weckwerth, T. M., Parsons, D. B., Koch, S. E., Moore, J. A., LeMone, M. A., Demoz, B. B., et al. (2004). An overview of the international H_2O project (IHOP_2002) and some preliminary highlights. *Bulletin of the American Meteorological Society*, *85*(2), 253–278. https://doi.org/10.1175/BAMS-85-2-253

Weisman, M. L., & Klemp, J. B. (1984). The structure and classification of numerically simulated convective storms in directionally varying wind shears. *Monthly Weather Review*, *112*(12), 2479–2498. https://doi.org/10.1175/1520-0493(1984)112<2479:TSACON>2.0.CO;2

Wheatley, D. M., & Trapp, R. J. (2008). The effect of mesoscale heterogeneity on the genesis and structure of mesovortices within quasi-linear convective systems. *Monthly Weather Review*, *136*(11), 4220–4241. https://doi.org/10.1175/2008MWR2294.1

Wilson, J. W., Trier, S. B., Reif, D. W., Roberts, R. D., & Weckwerth, T. M. (2018). Nocturnal elevated convection initiation of the PECAN 4 July hailstorm. *Monthly Weather Review*, *146*(1), 243–262. https://doi.org/10.1175/MWR-D-17-0176.1

Xie, Z., & Bueh, C. (2015). Different types of cold vortex circulations over Northeast China and their weather impacts. *Monthly Weather Review*, *143*(3), 845–863. https://doi.org/10.1175/MWR-D-14-00192.1

Xu, W., Zipser, E. J., Chen, Y.-L., Liu, C., Liou, Y.-C., Lee, W.-C., & Jou, B. J.-D. (2012). An orography-associated extreme rainfall event during TiMREX: Initiation, storm evolution, and maintenance. *Monthly Weather Review*, *140*(8), 2555–2574. https://doi.org/10.1175/MWR-D-11-00208.1

Xu, X., Xue, M., Wang, Y., & Huang, H. (2017). Mechanisms of secondary convection within a Mei-Yu frontal mesoscale convective system in eastern China. *Journal of Geophysical Research: Atmospheres*, *122*, 47–64. https://doi.org/10.1002/2016JD026017

Xue, M., Droegemeier, K., Wong, V., Shapiro, A., & Brewster, K. (1995). *Advanced regional Prediction System (ARPS) version 4.0 user's guide*. Center for Analysis and Prediction of Storms, University of Oklahoma.

Xue, M., Droegemeier, K. K., & Wong, V. (2000). The Advanced Regional Prediction System (ARPS)—A multi-scale nonhydrostatic atmospheric simulation and prediction tool. Part II: Model dynamics and verification. *Meteorology and Atmospheric Physics*, *75*(3-4), 161–193. https://doi.org/10.1007/s007030070003

Xue, M., Droegemeier, K. K., Wong, V., Shapiro, A., Brewster, K., Carr, F., et al. (2001). The Advanced Regional Prediction System (ARPS)—A multi-scale nonhydrostatic atmospheric simulation and prediction tool. Part II: Model physics and applications. *Meteorology and Atmospheric Physics*, *76*(1-4), 143–165. https://doi.org/10.1007/s007030170027

Xue, M., Kun, Z., Mingjung, W., Zhaohui, L., & Yongguang, Z. (2016). Recent significant tornadoes in China. *Advances in Atmospheric Sciences*, *33*(11), 1209–1217. https://doi.org/10.1007/s00376-016-6005-2

Xue, M., Luo, X., Zhu, K., Sun, Z., & Fei, J. (2018). The controlling role of boundary layer inertial oscillations in Meiyu frontal precipitation and its diurnal cycles over China. *Journal of Geophysical Research: Atmospheres*, *123*, 5090–5115. https://doi.org/10.1029/2018JD028368

Xue, M., & Martin, W. J. (2006). A high-resolution modeling study of the 24 May 2002 dryline case during IHOP. Part I: Numerical simulation and general evolution of the dryline and convection. *Monthly Weather Review*, *134*(1), 149–171. https://doi.org/10.1175/MWR3071.1

Xue, M., Qin, X., & Droegemeier, K. K. (1997). A theoretical and numerical study of density currents in nonconstant shear flows. *Journal of the Atmospheric Sciences*, *54*(15), 1998–2019. https://doi.org/10.1175/1520-0469(1997)054<1998:ATANSO>2.0.CO;2

Xue, M., Wang, D., Gao, J., Brewster, K., & Droegemeier, K. K. (2003). The Advanced Regional Prediction System (ARPS), storm-scale numerical weather prediction and data assimilation. *Meteorology and Atmospheric Physics*, *82*(1-4), 139–170. https://doi.org/10.1007/s00703-001-0595-6

Xue, M., Zong, J., & Droegemeier, K. K. (1996). *Parameterization of PBL turbulence in a multi-scale non-hydrostatic model* (pp. 363–365). Paper presented at 11th AMS Conference on Numerical Weather Prediction, American Meterogical Society, Norfolk, VA.

Zhang, H., & Zhai, P. (2011). Temporal and spatial characteristics of extreme hourly precipitation over eastern China in the warm season. *Advances in Atmospheric Sciences*, *28*(5), 1177–1183. https://doi.org/10.1007/s00376-011-0020-0

Zhang, L., & Li, Z. (2009). A summary of research on cold vortex over northeast China. *Climte Environmental Research* (in Chinese, *14*, 218–228.

Zhu, K., & Xue, M. (2016). Evaluation of WRF-based convection-permitting multi-physics ensemble forecasts over China for an extreme rainfall event on 21 July 2012 in Beijing. *Advances in Atmospheric Sciences*, *33*(11), 1240–1258. https://doi.org/10.1007/s00376-016-6202-z

Zhu, K., Xue, M., Zhou, B., Zhao, K., Sun, Z., Fu, P., et al. (2018). Evaluation of real-time convection-permitting precipitation forecasts in China during the 2013–2014 summer season. *Journal of Geophysical Research: Atmospheres*, *123*, 1037–1064. https://doi.org/10.1002/2017JD027445

Ziegler, C. L., Lee, T. J., & Pielke, R. A. (2010). Convective initiation at the dryline: A modeling study. *Monthly Weather Review*, *125*, 1001–1026.